ECAP-2020-009

Calibration of Photomultiplier Tubes for Intensity Interferometry at H.E.S.S.

Master's Thesis in Physics

Presented by
Naomi Vogel
November 9, 2020

Erlangen Centre for Astroparticle Physics
Friedrich-Alexander-Universität Erlangen-Nürnberg

Supervisors:
Prof. Dr. Gisela Anton
Prof. Dr. Stefan Funk

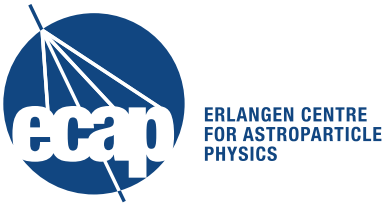

Contents

Chapter 1

Introduction

Intensity Interferometry offers the possibility to measure the angular size of stars, which has been the main goal of optical astronomy for many years. A high resolution is typically achieved by amplitude interferometers, which merge the light from telescopes at different positions. This requires high optical precision and the length of the baselines is limited by atmospheric turbulences to some 100 m. In contrast, intensity interferometry measures temporal correlations of arrival times between photons captured at different telescopes to achieve the second-order coherence of light (intensity) [1]. This concept circumvents the issues of atmospheric turbulences and optical imperfections of telescopes, promising the use of very long baselines. Hanbury Brown and Twiss were the first to build an intensity interferometer in the late 1950s to measure stellar sizes [2, 3].
Although so far only a few stars with tens of milliarcseconds (mas) in diameter have been revealed, baselines of several kilometers will enable to observe stars with sub-mas angular resolution. This improvement of spatial resolution could be achieved by the Cherenkov Telescope Array (CTA) with its huge light-collecting area and large telescope baselines for future optical astronomy measurements.

In this thesis, a measurement procedure for first current correlation tests at the H.E.S.S. telescopes is developed. At first, the waveforms of two types of photomultiplier tubes (PMT) are investigated thoroughly and two methods to determine the incoming photon rate are established. Furthermore, a calibration of the PMT at various voltages is performed and its pulse shape is investigated. Then, these findings are combined into the development of the measurement procedure including calibration and correlation measurement.

Chapter 2

Intensity Interferometry

Contents

In this chapter, the background for the thesis is reviewed. At first, the historical background considering intensity interferometry is presented, such as how traditional telescopes were replaced by Michelson interferometers for angular resolution measurements and the development of intensity interferometry, which can be extended at modern Cherenkov telescopes. This leads to the Cherenkov telescope array H.E.S.S., which actually studies cosmic rays and radiation in the cosmos, and the planned H.E.S.S. campaign. The chapter proceeds with the theoretical background of intensity interferometry. The term coherence is introduced, since coherence effects play a great part in intensity interferometry, and its evaluation via first- and second-order correlation functions. These can be calculated with the help of two theorems if certain parameters are known. The source geometry can also be determined from measuring the correlation functions.

2.1 Historical Background

When looking and describing the night sky, all stars (except for the sun) are referred to as “little” stars, believing they are all more or less equal in size but different

in luminosity. However, the starlight we observe is actually due to atmospheric fluctuations, which also create the twinkling of the stars, and has nothing to do with the angular size. Except for close giant stars, telescopes have not been able to measure the angular diameter of small stars, due to their diffraction limit. The intensity pattern of a telescope with circular aperture D has its maximum at $\theta = 0$ and its first minimum at $\theta_{\min}$ with:

$$\sin\theta_{\min} = 1.22\frac{\lambda}{D} \tag{2.1}$$

and λ being the wavelength [4]. This formula is used to calculate the resolving power of telescopes, meaning the bigger the aperture D the better the angular resolution. However, such big telescopes have yet to be built, which is both challenging and expensive.

Interferometry is the standard method to measure the angular size of stars to this day and the origin is the Michelson interferometer. A Michelson interferometer is composed of two telescopes observing the same star but installed at a certain distance, baseline d, from each other. It uses amplitude interferometry, which is very challenging. The timing of the detected light, the amplitudes, at both detectors has to be coincident, meaning the path between the detectors and the resulting interference pattern has to be adjustable, as the star moves along the night sky. Therefore, a high precision in scale of the optical or infrared wavelength is necessary, which on the other hand limits the length of the baseline to only a few hundred of meters.

To escape these restrictions, a new method, called intensity interferometry, was first devised by Hanbury Brown and Twiss in 1956. To measure the angular diameter of stars, the time of arrival of photons in coherent beams of light is correlated. The basic equipment they used to determine the diameter of Sirius is shown in Figure 2.1. Two mirrors focus starlight on photomultipliers, which transform the recorded intensity into electrical signals. The signals are amplified and multiplied. [5]

For further measurements of more than 30 stars, carried out between 1964 and 1972, they used the Narrabri Stellar intensity interferometer. Figure 2.2 shows a circular railroad tray of 188 m diameter on which two telescopes of 6-7 m diameter are mounted. They were able to measure an angular size as small as (0.41 ± 0.03) mas with a maximum baseline of 144.3 m. [2, 3]

It is important that when measuring the intensity correlation of light between the two spatially separated telescopes, there is no time delay in the time of arrival of the photons. Since the telescopes are only connected electronically and not optically, the noise budget relates to the electronic time resolution of a few nanoseconds with

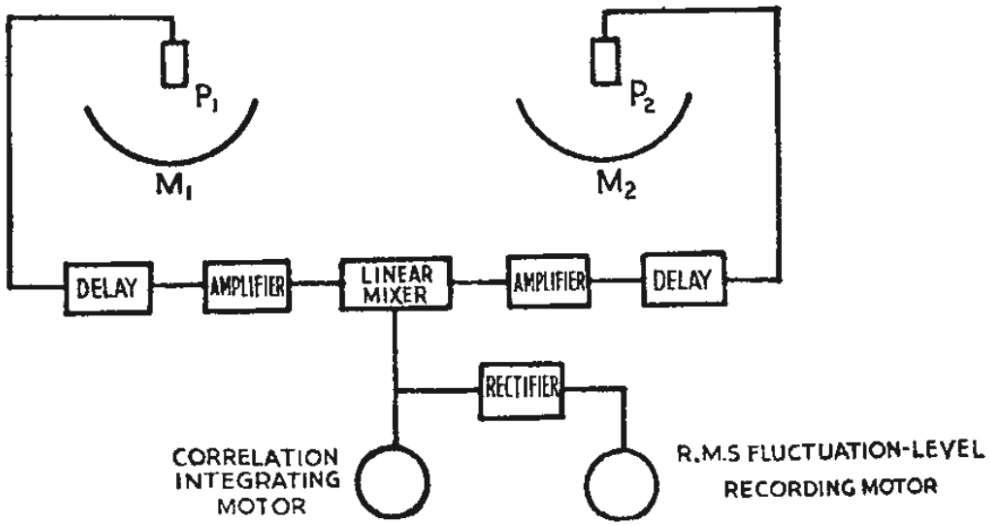

Figure 2.1: Schematic layout of the experimental setup used by Hanbury Brown and Twiss. [5]

corresponding light-travel distances of one meter. [6]
This has the big advantage that the method is almost insensitive to atmospheric effects and optical faults of telescopes, allowing long baselines. [7]
However, with the electronics at the time, the method was challenging, also due to lack of sensitivity, which required large-area collectors and very long integration times. Thus, it has not been further pursued in astronomy but has been widely applied in particle physics. [8]
In recent years, many efforts have been made to revive intensity interferometry in astronomy. Progress has not only been made in photonic technologies but also in high-speed electronics, which holds new potential considering long baselines in the range of several km. This technique is based on the use of large Cherenkov telescope arrays, such as H.E.S.S. [7, 8]

2.2 Intensity Interferometry at H.E.S.S.

H.E.S.S. – **H**igh **E**nergy **S**tereoscopic **S**ystem – is an installation of Imaging Atmospheric Cherenkov Telescopes, that studies cosmic rays in the energy range of GeV to TeV. It was also named after Victor Hess, who won the Nobel Prize in physics in 1936 for discovering cosmic radiation. The telescopes are based in Namibia, near the Gamsberg mountain, a location which is established for its favorable optical conditions. H.E.S.S. is made up of four telescopes of Phase I, which were inaugurated in 2004. To expand the energy analysis towards lower

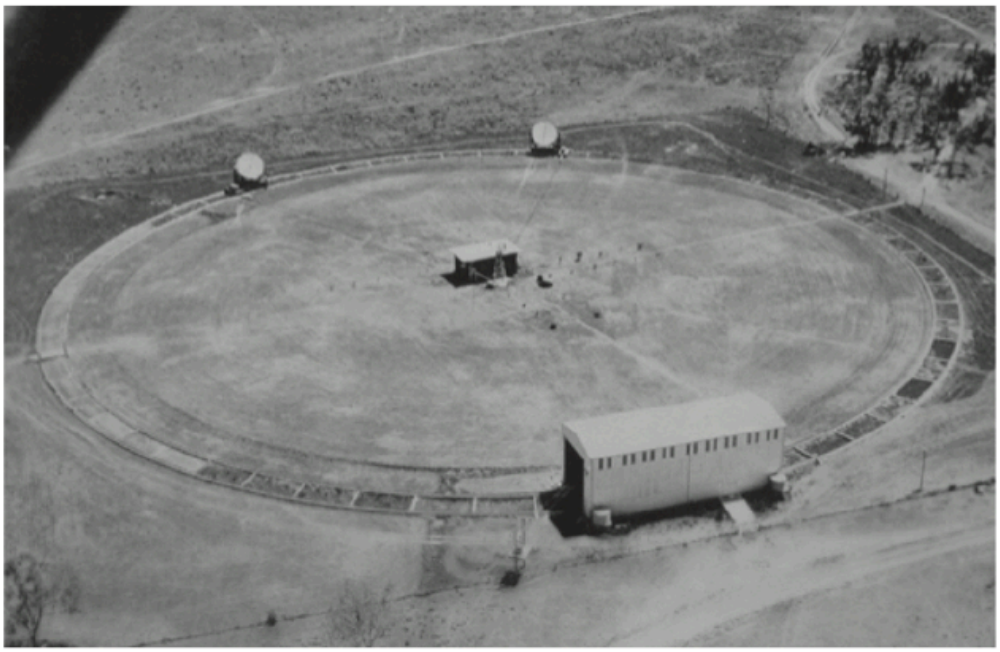

Figure 2.2: The Narrabri Stellar intensity interferometer composed of two telescopes mounted on a circular rail track to vary the baseline. [9]

energies and enhance sensitivity, a fifth telescope Phase II, which is much larger, was ready to go in 2012. In September 2020, H.E.S.S. celebrated its 20th anniversary of groundtaking. The collaboration, which operates the H.E.S.S. observatory, includes 13 different countries with about 40 scientific institutions. [10]

The telescopes are aligned in such a way that they observe the same air shower. The four telescopes of Phase I have a diameter of 12 m and constitute a square with 120 m side length, to allow a stereoscopic reconstruction of the shower geometry. The total mirror area per telescope is $108\,\mathrm{m}^2$, which is segmented into 382 round mirror facets. Each facet can be adjusted for alignment and they are focused for an object distance of about 10 km, which is the typical height for an air shower. The fifth larger telescope, with a diameter of 28 m, was built in the center of the square expanding the energy range, sensitivity and angular resolution. The total mirror area is $614\,\mathrm{m}^2$, which is made of 875 hexagonal facets. [10, 11]
The main goal of the H.E.S.S. experiment is to investigate the non-thermal universe. A lot of the radiation found in the cosmos and the Earth is thermal radiation, which comes from hot sources such as stars. But some particle populations are non-thermal, e.g. cosmic rays, energies of which reach up to $10^{20}\,\mathrm{eV}$ and higher. Nevertheless, a great deal of this area of the universe is still unexplored, which is why H.E.S.S. provides the experimental basis for an improved understanding.

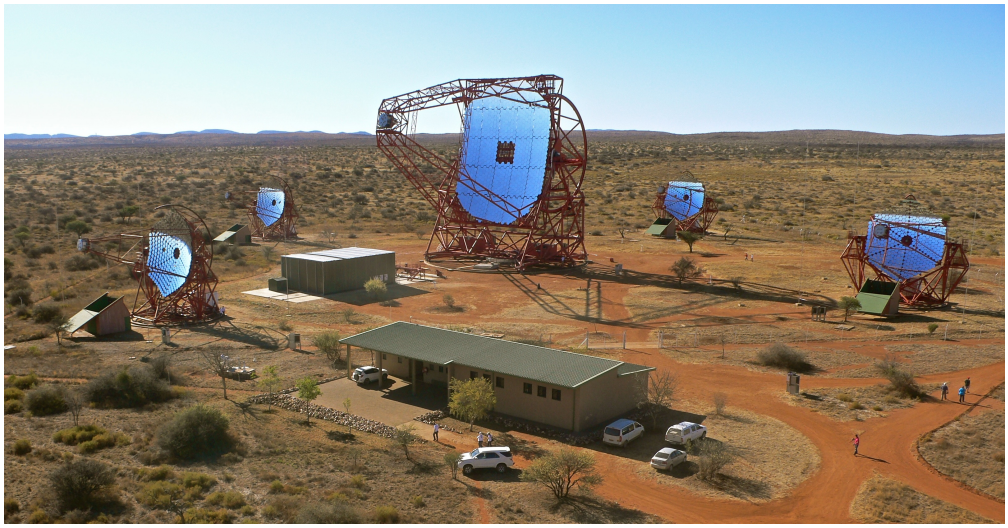

Figure 2.3: The H.E.S.S. experiment with its four Phase I telescope and bigger Phase II telescope in the middle. [11]

As described above, the telescopes have huge mirror areas having the advantage of getting high photon rates and good statistics, which are two important features for the planned H.E.S.S. campaign. It includes doing correlation measurements of various stars with two of the telescopes of Phase I, since they have a long baseline, which is of interest for intensity interferometry measurements. The goal is to have two spatially separated telescopes the PMT setups will be mounted on. Each PMT will record the intensity of the observed stellar object and both obtained signals will be correlated after.

2.3 Theoretical Background

2.3.1 Coherence

Coherence plays an important role when talking about intensity interferometry, since no interference patterns are visible without it.
Coherence is the property that describes the "stability of light" [4]. Light is coherent when its wave packets have a constant phase relation, which makes it possible for them to interfere. [12]
Physics distinguishes between spatial and temporal coherence. Due to their design, certain light sources, e.g. lasers, already show spatial and temporal coherence. Coherence is specified by its coherence time τ_c and coherence length L_c.

The coherence time is the time period within which the phase of the wave packet continues to be stable, saying that the phase at a given point within this interval can be predicted. The coherence time is inversely proportional to the spectral bandwidth $\Delta\nu$ of the light source [4]:

$$\tau_c = \frac{1}{\Delta\nu} \tag{2.2}$$

If an ideal monochromatic light source is used, the frequency would not change over time ($\Delta\nu = 0$) and the coherence time would be infinite. Considering a quasi-monochromatic light source, frequency of which fluctuates around a mean frequency, $\Delta\nu$ and τ_c are finite, meaning that the wave has a fixed phase relation within τ_c.

Because of the inverse relation $\nu = c/\lambda$, the coherence time is described by the wavelength bandwidth $\Delta\lambda$. The spectral bandwidth is thus dependent on the center wavelength λ_0. For small bandwidths, however, a linear approximation can be made [13]:

$$\Delta\nu = \left.\frac{d\nu}{d\lambda}\right|_{\lambda_0} \cdot \Delta\lambda = (-)\frac{c}{\lambda_0^2}\ \Delta\lambda \tag{2.3}$$

This transfers to the coherence time as follows:

$$\tau_c = \frac{\lambda_0^2}{c\Delta\lambda} \tag{2.4}$$

The broader the wavelength bandwidth the shorter the coherence time. Therefore, it is crucial to optically filter the incoming light from the telescopes or lab setup.

2.3.2 Correlation Functions

Further important terms in intensity interferometry are the normalized n-th order correlation functions, which are used to describe coherence effects.
Since the wave packets of coherent light present a fixed phase relation, their electric field amplitudes are correlated. This is displayed in the first-order correlation function [14]:

$$g^{(1)}(R_1, R_2, \tau) = \frac{\langle E^*(R_1, r) \cdot E(R_2, t+\tau)\rangle}{\langle E^*(R_1, t) \cdot E(R_1, t)\rangle} \tag{2.5}$$

where R_1 and R_2 are two positions in space and τ is a time difference. The electric field at position R_1 and time t is correlated with the electric field at position R_2 and time $t + \tau$. The field is then averaged over time, which is indicated by the brackets $\langle\rangle$ [14]:

$$\langle E(t)\rangle = \frac{1}{T}\int_0^T E(t)\,\mathrm{d}t \tag{2.6}$$

where T is relatively big in comparison to τ. Therefore, the time t is not a parameter of the $g^{(1)}$ function but instead the time difference τ. The denominator in Equation 2.5 serves as normalization, where in this case position R_1 is used. Since $E^*E = I$ holds, the normalization can be seen as a time averaging over the intensity at R_1 or R_2. The choice of the position is irrelevant because the intensity at R_1 does not differ from the intensity at R_2. When considering stars, the distance between detector and star is a lot bigger than the distance between two detectors. In intensity interferometry, only the intensities are measured and correlated, not the amplitudes. This is why the second-order correlation function is of interest and is defined as [14]:

$$g^{(2)}(R_1, R_2, \tau) = \frac{\langle I(R_1, t) \cdot I(R_2, t+\tau)\rangle}{\langle I(R_1, t)\rangle \cdot \langle I(R_2, t+\tau)\rangle} \tag{2.7}$$

where $E^*E = I$ was used to simplify the equation. When regarding the intensity as fluctuations around the average intensity, $I(t) = \langle I(t)\rangle + \Delta I(t)$, the $g^{(2)}$ function can be written as:

$$g^{(2)}(\mathrm{R}_1, \mathrm{R}_2, \tau) = 1 + \frac{\langle \Delta \mathrm{I}_1 \cdot \Delta \mathrm{I}_2\rangle}{\langle \mathrm{I}_1\rangle \cdot \langle \mathrm{I}_2\rangle} \tag{2.8}$$

As for coherence, correlations can be treated separately in space and time. The spatial correlation is achieved by setting $\tau = 0$ and the temporal correlation is achieved by observing at the same positions $R_1 = R_2$. Both correlation types will be covered in the next sections.

The $g^{(2)}$ function is dependent on the intensity fluctuations ΔI. Three cases are distinguished:

- $\langle \Delta I_1 \Delta I_2 \rangle = 0$ and $g^{(2)} = 1$
  For coherent light, the intensity fluctuations are totally random and the product results in zero, meaning no correlation signal is measured.

- $\langle \Delta I_1 \Delta I_2 \rangle > 0$ and $g^{(2)} > 1$
  For chaotic light, photons often appear almost simultaneously, $\tau = 0$, which is referred to as bunching effect. The intensity fluctuations are mostly of the same sign. This case is the main focus in intensity interferometry.

- $\langle \Delta I_1 \Delta I_2 \rangle < 0$ and $g^{(2)} < 1$
  The anti-bunching effect means that photons don't appear simultaneously, resulting in the product of the intensity fluctuations having a negative sign. This can happen for a single atom. After emitting a photon, it takes time to reexcite to emit another photon. The first photon is only registered by one detector, whereas the other detector measures a negative fluctuation ΔI.

Considering thermal light, the **Siegert relation** connects the first- and second-order correlation functions [14]:

$$g^{(2)}(R_1, R_2, \tau) = 1 + |g^{(1)}(R_1, R_2, \tau)|^2 \tag{2.9}$$

This is the case for a thermal light source, which consists of a large number of atoms, whose electromagnetic waves interfere at the observer. Since there are only theorems associating the $g^{(1)}$ function with the physical properties of the light source, it would be possible to deduce these properties by measuring the $g^{(2)}$ function only and with the help of the Siegert relation. But these properties cannot be derived analytically by simply measuring the $g^{(2)}$ function. There are reasonable educated guesses though, e.g. that stars are more round than an abstract shape, that allow a precise estimation of many of these properties.

2.3.3 Van Cittert-Zernike Theorem

Suppose a planar extended incoherent light source, the van Cittert-Zernike theorem describes the link between the spatial intensity distribution of the source and the first-order correlation function [15]:

$$g^{(1)}(\boldsymbol{r}_1, \boldsymbol{r}_2) = \exp(ik(r_2 - r_1)) \frac{\int_\sigma I(\boldsymbol{r}' x) \exp(ik(\boldsymbol{s}_2 - \boldsymbol{s}_1)\boldsymbol{r}') \, \mathrm{d}^2\boldsymbol{r}'}{\int_\sigma I(\boldsymbol{r}') \, \mathrm{d}^2\boldsymbol{r}'} \tag{2.10}$$

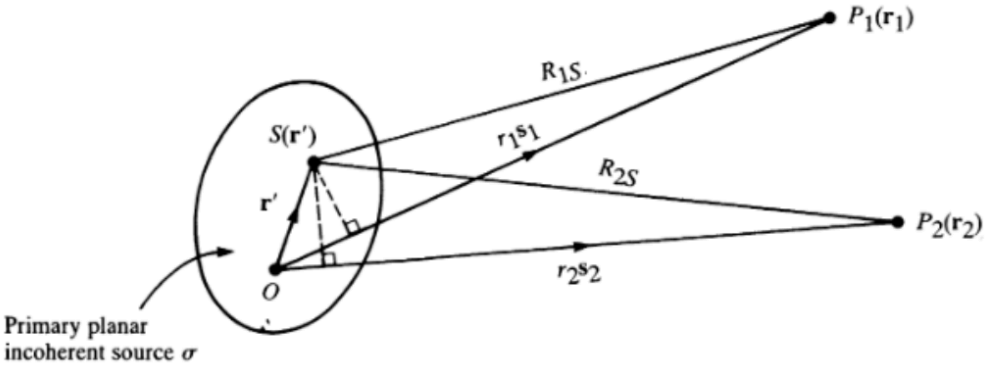

Figure 2.4: Geometry for the Cittert-Zernike theorem and Equation 2.10. [15]

Figure 2.4 presents the equation graphically. The geometry of the source origin O is σ and its intensity $I(\boldsymbol{r}')$ at position $\boldsymbol{r}$. Both detectors P_1 and P_2 are positioned at $\boldsymbol{r}_1 = r_1\boldsymbol{s}_1$ and $\boldsymbol{r}_2 = r_2\boldsymbol{s}_2$ with $r_j = |\boldsymbol{r}_j|$ being the distance between them.
Apart from the the first factor in Equation 2.10 and the normalization in the denominator, the $g^{(1)}$ function is proportional to the two-dimensional Fourier transformation of the intensity distribution of the light source. Therefore, measuring the first-order correlation function allows to draw conclusions regarding the geometry of the source, which is the technique of amplitude interferometry.

The Fourier transform also serves to calculate the Fraunhofer diffraction pattern. If an aperture is illuminated by a coherent light source, it forms a diffraction pattern. The first-order correlation function of an incoherent light source in the distant field shows the same shape as the mentioned pattern.
Considering a slit aperture first, the $g^{(1)}$ function is outlined by a sinc-function $\mathrm{sinc}(x) = \sin(x)/x$. The slit with width s and distance d to the detectors P_1 and P_2 in the observer plane B is shown in Figure 2.5. The resulting pattern has its maximum at P_1 and its first minimum at P_2 with distance d_{12} to P_1. The minimum of the $g^{(1)}$ function is also the criterion of the size of the coherence cell, which is the goal to calculate.
The graphic with the help of the small-angle approximation shows that:

$$\tan(\alpha) = \frac{d_{12}}{d} \quad \rightarrow \quad d_{12} = \tan(\alpha) \cdot d = \alpha \cdot d \tag{2.11}$$

Since the first minimum is of interest, d_{12} results in:

$$d_{12} = \frac{\lambda}{s} \cdot d \tag{2.12}$$

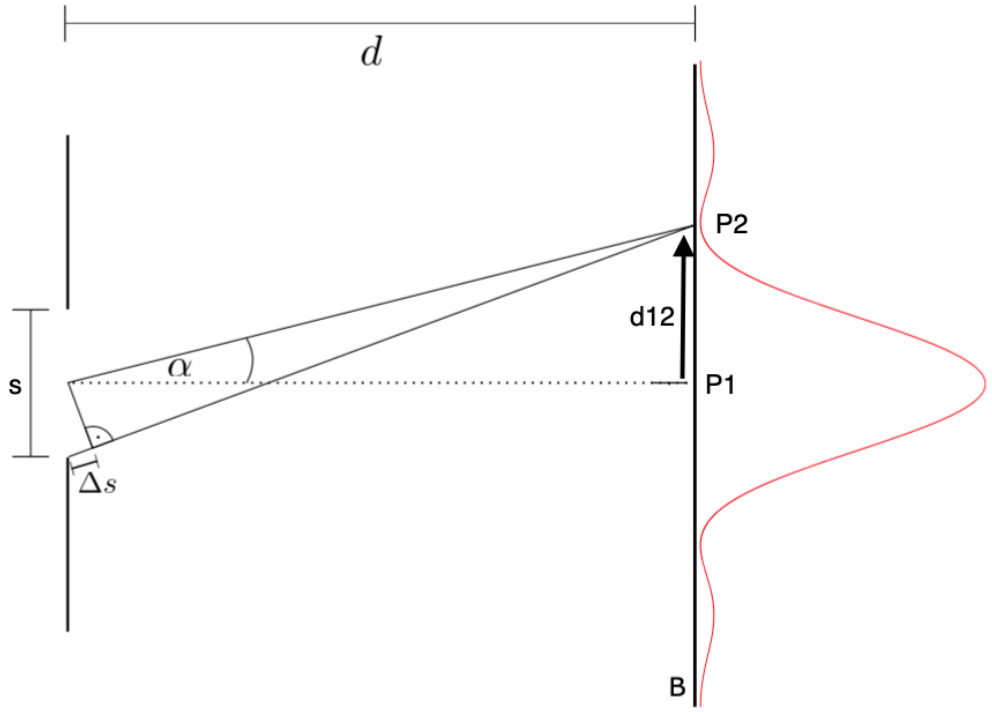

Figure 2.5: Geometry of a slit aperture. The interference pattern in the observer plane B is shown in red. Sketch is modified from [16].

This means that the larger the wavelength λ or distance d the bigger the coherence cell. But if the width s of the slit increases, the coherence cell decreases.

Considering a circular aperture with a diameter s, the $g^{(1)}$ function is described via the first-order Bessel function J_1 [14]:

$$g^{(1)}(d_{12}) = \frac{2J_1(X)}{X} \tag{2.13}$$

where $X = \pi s d_{12}/d\lambda$, with the distance d from the source to the detectors. Although the $g^{(1)}$ function cannot be measured directly, it can be calculated via the Siegert relation from the $g^{(1)}$ function. Additionally, a factor 1.22 is added when calculating the first minimum of the $g^{(1)}$ function:

$$d_{12} = 1.22 \cdot \frac{\lambda d}{s} \tag{2.14}$$

2.3.4 Wiener-Khinchin Theorem

The relation between the temporal first-order correlation function $g^{(1)}(\tau)$ and the normalized spectral intensity distribution $F(\omega)$ is known as the Wiener-Khinchin theorem [14]:

$$F(\omega) = \frac{1}{2\pi} \int_{-\infty}^{+\infty} g^{(1)}(\tau) \exp(i\omega\tau)\, \mathrm{d}\tau \tag{2.15}$$

with $F(\omega)$ being the Fourier transform of the $g^{(1)}$ function. If using the back transformation, the $g^{(1)}(\tau)$ function can be calculated from the spectral intensity distribution:

$$g^{(1)}(\tau) = \int_{-\infty}^{+\infty} F(\omega) \exp(-i\omega\tau)\, \mathrm{d}\omega \tag{2.16}$$

In this thesis, an interference filter with $\Delta\lambda = 2\,\mathrm{nm}$ was used to filter the light of the LED with $\lambda = 465\,\mathrm{nm}$. It operates similar to a rectangular filter with bandwidth $b = \Delta\omega$, which only passes frequencies in an interval $[\omega_0 - {}^{\Delta\omega}/_2 : \omega_0 + {}^{\Delta\omega}/_2]$ around a central frequency ω_0. [13]
Since the amplitude is normalized $1/\Delta\omega$, $\int F(\omega)\mathrm{d}\omega = 1$ holds. Including this into Equation 2.16, the $g^{(1)}(\tau)$ function results in:

$$g^{(1)}(\tau) = \frac{1}{\Delta\omega} \int_{\omega_1}^{\omega_2} \exp(-i\omega\tau)\, \mathrm{d}\omega = \exp(-\tau\omega_0)\, \mathrm{sinc}\left(\frac{\tau\Delta\omega}{2}\right) \tag{2.17}$$

with $\omega_1 = \omega_0 - \Delta\omega/2$ and $\omega_2 = \omega_0 + \Delta\omega/2$.
Remembering the Siegert relation, the $g^{(2)}$ function results in:

$$g^{(2)}(\tau) = 1 + |g^{(1)}(\tau)|^2 = 1 + \left|\mathrm{sinc}\left(\frac{\tau\Delta\omega}{2}\right)\right|^2 \tag{2.18}$$

It shows the same result as the spatial $g^{(2)}$ function and is independent of the wavelength of the light source. Looking at its range, the $g^{(2)}$ function reaches 2 for $\tau = 0$, whereas it reaches 1 for large τ.
Since we have been looking for the first minimum before, it lies at $\tau_1 = 2\pi/\Delta\omega$, with $\tau_1\Delta\omega/2 = \pi$.

Returning to the LED and interference filter, where the bandwidth $\Delta\omega = b = \Delta\lambda$ and $\lambda = 2\pi c/\omega$, the first minimum lies at:

$$\tau_1 = \frac{\lambda_0^2}{c\Delta\lambda} \tag{2.19}$$

This means that the smaller the optical bandwidth the broader the $g^{(2)}$ function, referring to the time period in which a correlation signal can be measured.
It corresponds to Equation 2.4 in subsection 2.3.1, where the same relation between coherence time and optical bandwidth is established.

Considering the setup, which was used in this thesis, an interference filter with $\Delta\lambda = 2\,\text{nm}$ at $\lambda_0 = 465\,\text{nm}$, the first minimum lies at:

$$\tau_1 = \frac{(465\,\text{nm})^2}{c \cdot 2\,\text{nm}} = 3.6 \cdot 10^{-13}\,\text{s} = 0.36\,\text{ps} \tag{2.20}$$

This states that in the range of $\pm 0.36\,\text{ps}$ photons are correlated and a correlation signal is measured. A sufficiently good time resolution to study such effects in detail is difficult to achieve experimentally. The shape of the $g^{(2)}$ function at $\tau \approx 0$ is only intensified minimally, whereas for $\tau \neq 0$ it stays 1 within statistical fluctuations, if there is no electrical noise producing signals at other time differences. If the time resolution were more precise, the signal wouldn't spread over several measurement bins, which would make it easier to detect it. In order not to distort the anyhow small signal, the mentioned shot noise has to be as small as possible. Since it is Poisson distributed, long measurement time and high photon rates would actually decrease noise fluctuations.

Chapter 3

Electronic Setup

Contents

This chapter addresses the components used for the measurements in this thesis and discusses their relevance. Since the setups for the different measurements vary slightly, they are introduced within each chapter for the specific measurement. However, the following three components are installed in every setup. The functionality of a photomultiplier, which detects the photons, is discussed and the two different photomultipliers used within this thesis are presented including their specific attributes. The two different amplifiers, which amplify each photomultiplier's signal, are featured. And the functionality of the digitizing card and its setting options are explained.

3.1 Photomultiplier

Photomultiplier tubes (PMT) are versatile devices used to detect photons that offer high sensitivity and fast response. There are three operating principles of photodetectors: external photoelectric effect, internal photoelectric effect and thermal types [17]. PMTs operate via the external photoelectric effect, meaning that electrons are emitted from a metal or semiconductor surface when it is exposed to light. [17]

A typical PMT consists of an entrance window, a photocathode, focusing electrodes, an electron multiplier and an electron collector (anode) all within a vacuum tube. A schematic construction of a PMT is shown in Figure 3.1. The basic role of a PMT is to convert light into an electrical signal, which is then amplified by emission of secondary electrons. The more detailed process starts with light passing through the entrance window. The incident photons excite the electrons in the photocathode, which are then emitted as photoelectrons into vacuum. The photoelectrons are focused and accelerated by the focusing electrodes towards the electron multiplier, which consists of several dynodes. Hitting the first dynode, the photoelectrons are multiplied via secondary emission. This process is repeated at each dynode. The anode collects the multiplied secondary electrons after the last dynode and provides an output signal. Due to this operating principle, PMTs present excellent low noise, extremely high sensitivity and ultra-fast response. [17, 18]
PMTs are defined by several characteristics, some of which are described in the following. By repeating the process of secondary emission at each dynode, a high current amplification (gain) is attained. This leads to a large output current while only a small current is observed at the photocathode. The gain is defined by an average secondary emission (multiplication) factor δ of each dynode. A PMT with n dynodes has a current amplification of $G = \delta^n$. [18]
Quantum efficiency (QE) is the probability to trigger an electron, meaning the ratio of the number of photoelectrons emitted from the photocathode to the number of incident photons. The collection efficiency (CE) is the probability to collect the triggered electron at the first dynode. And the detection efficiency (DE) is the ratio of the number of detected events to the number of incident photons. Given these parameters, the DE can also be expressed as the product of the QE and CE. [17, 18]

The first detector used in this thesis is a PMT R12992-100 from Hamamatsu with an effective area with a diameter 30 mm. The PMT has a QE of 32% at a wavelength of 350 nm and approximately 30% at 450 nm. The PMT is also referred to as FlashCam PMT in this thesis, since they are used for the FlashCam project. A circuit diagram is shown in Figure 3.2, where seven dynodes and two HV channel connections (A and B) can be seen, channel A providing all dynodes and channel B the last two dynodes, 6 and 7. [19]

The second PMT is a R11265U-300 from Hamamatsu with an effective area of $(23 \times 23)\,\mathrm{mm}^2$. It has a QE of 39% at 420 nm and approximately 33% at 450 nm. It is referred to as Hamamatsu PMT in this thesis. Figure 3.3 illustrates a circuit diagram, which shows twelve dynodes and two HV channel connections. The main voltage (HV) providing all dynodes and the booster voltage providing the rear four dynodes. The maximum current, which is allowed to flow through the PMT, is limited to 100 µA. [20]

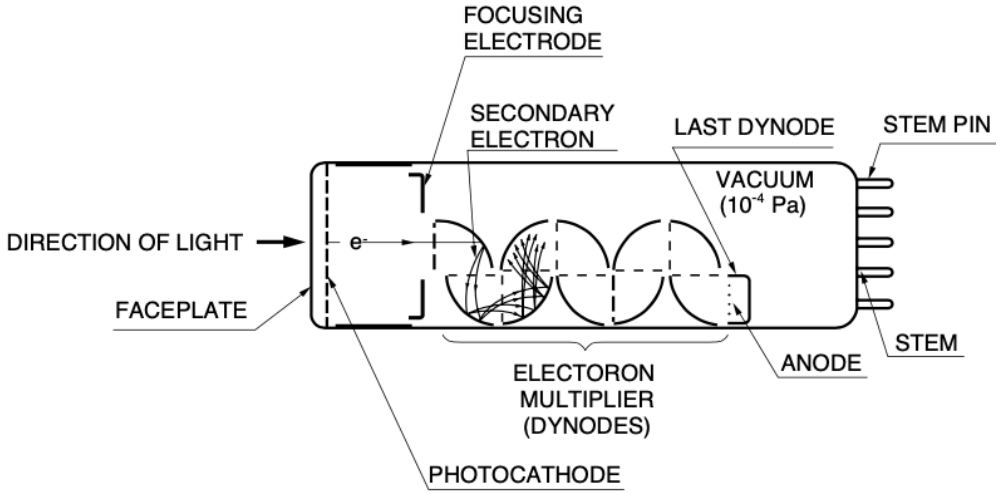

Figure 3.1: Schematic cross section of a PMT. [18]

Comparing the two PMTs, the Hamamatsu PMT has more dynodes than the FlashCam PMT, resulting in a higher gain. It also features a higher QE around the wavelength range for blue light. And it has a higher internal amplification, meaning an amplifier with a lower amplification factor can be installed, resulting in less noise amplification.

3.2 Amplifier

To amplify the FlashCam PMT signal, the amplifier model VT120 by ORTEC is used. It is a high-performance, wider bandwidth preamplifier developed for boosting very fast linear signals from PMTs [21]. The amplifier provides a fast rise time over a bandwidth of 10-350 MHz enabling a high time resolution. It is AC coupled normalizing the signal to a mean of zero. [21]

The amplifier type TA1000B-200 by FAST is used to amplify the Hamamatsu PMT. It is a fast, very low noise preamplifier and is DC coupled, not influencing the signal except for an offset, which can be set to zero. The amplifier provides a fast rise time with a gain of 46 dB over a small signal bandwidth of 400 MHz. This resembles an amplification factor of 200, which is too high for the Hamamatsu PMT, since it has a higher internal amplification than the FlashCam PMT. The amplifier was remodeled to achieve an amplification factor of 10. [22, 23]
The amplified PMT signal is transmitted directly to the digitization card.

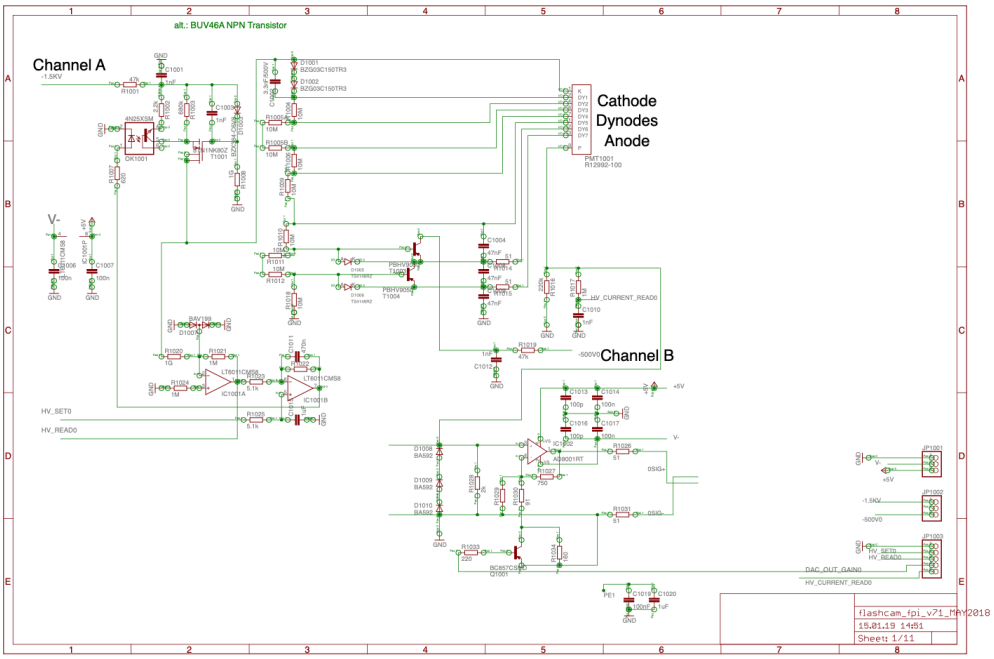

Figure 3.2: Circuit diagram of the FlashCam PMT. Channel A is connected to all dynodes, whereas channel B is only connected to the last two dynodes.

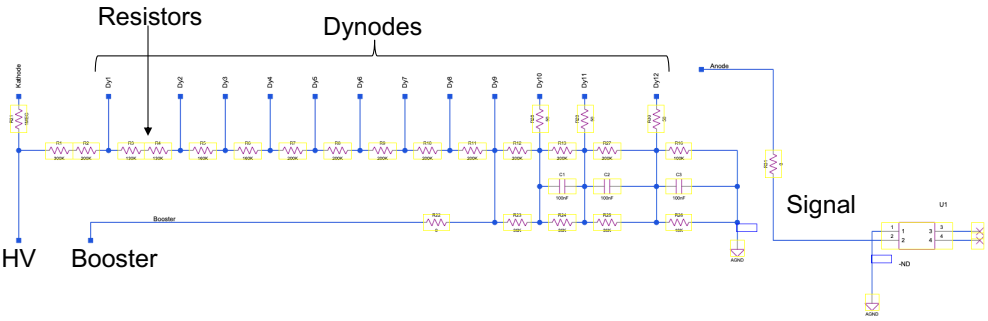

Figure 3.3: Circuit diagram of the Hamamatsu PMT. The HV is connected to all dynodes, whereas the Booster is only connected to the last four dynodes.

3.3 Digitization Card

The digitization card M4i.2212-x8 by Spectrum, referred to as Spectrum card in this thesis, is relevant for high speed data acquisition. It has four input channels, which can be connected to the amplifiers to analyze the PMT signals. It can sample at rates up to 1.25 GS/s with a maximum bandwidth of up to 500 MHz [24]. The used software support is the program "SBench 6", which is an easy-to-use graphical operating software for Spectrum cards. In the program the voltage range can be set to $\pm 40, \pm 100, \pm 200$ and ± 500 mV for each channel. The internal sampling clock was set to 0.8 ns or 1.6 ns for this thesis, which stands for the time difference between each sampling bin. And the input mode was set to 2 GS/s. For generating a waveform plot, 100 000 data points of the 2 GS file are taken, leading to a 80 µs long file for a 0.8 ns time binning and a 160 µs long file for a 160 ns time binning. The program presents the amplitude, y-axis, in ADC counts, which can then be converted into mV via the set voltage range. Therefore, it is important to know that the program ranges 127 ADC counts in both positive and negative direction. For example, a voltage range ± 100 mV is set. [24]
To convert 10 ADC counts into mV the following equation is used:

$$\frac{10\,\text{ADC} \cdot 100\,\text{mV}}{127} = 7.87\,\text{mV} \tag{3.1}$$

Chapter 4

Systematic Waveform Investigations Using the FlashCam PMT

Contents

This chapter addresses the characterization for rate measurements of a FlashCam PMT. The characterization is based on several measurements conducted at different photon rates and their analysis via python programs.
First, the background for this chapter is described and how it will help for future measurements and for the planned H.E.S.S. campaign. Second, the used setup with an LED as a light source is presented. Rate measurements with a FlashCam PMT and different discrepancies concerning the PMT's gain and the obtained results for photon pulse heights are introduced. For further investigations, waveforms were simulated to function as a comparison to the real data. Although solutions were found for the disagreements between real and simulated measurements, the FlashCam PMT with the used amplifier is not suitable for rate and correlation measurements at the H.E.S.S. telescopes. The reason is explained in the last section where measurements taken at the Medium-Sized Telescope prototype (MST) in Adlershof, Berlin are presented.

4.1 Measurement Berlin 2019

In summer 2019, the Intensity Interferometry research group at ECAP took measurements at the Medium-Sized Telescope (MST) prototype in Adlershof, Berlin. The results exposed two main issues, which had to be investigated thoroughly in the lab.
The measurements in Berlin were carried out with the FlashCam PMT, which was connected to a power supply by one channel. Pulse height histograms were analyzed, which show the count rate of photon pulses with a certain amplitude against the pulse height. They revealed that the PMT had saturation effects, especially for rates higher than 50 MHz, which is inconvenient for measurements of stars, where 200-500 MHz are expected. Additionally, the obtained waveform of the PMT revealed a baseline shift towards positive values for higher rates, which had to be prevented. These were two issues, which can be established by looking at the measured waveforms and the pulse height histogram via measurements taken in the lab with an LED and neutral density filters to create various rates.
Another issue was finding a reliable method to determine the exact incoming rate, which turned out to be deficient for high rates. In this thesis, several methods to determine the incoming rate are presented, which go hand in hand.

4.2 LED Setup

The first rate measurements were taken using the setup shown in Figure 4.1 with a schematic layout illustrated below. The light source is an LED with a center wavelength of $\lambda = 570\,\text{nm}$. LEDs have a broad natural bandwidth and since the LED exhibits similar properties to a star, it is an appropriate light source to simulate measurements with a star in the lab. A pinhole with a diameter of 75 µm is set in front of the LED to reduce stray light. In order to achieve different rates, various combinations of neutral-density (ND) filters are installed in front of the LED, since the filters reduce the amount of incoming light depending on their transmission value. The used ND filters are numbered with their optical densities 20, 13, 10, 6, 5, 2, 1, with $20 \mathrel{\widehat{=}} 2.0$ and having the highest transmission value, meaning decreasing the incoming light the most. The combinations and their transmission are listed in Table 4.1. The reduced intensity of the LED is guided through an interference filter with FWHM $\Delta\lambda = 2\,\text{nm}$ centered at $\lambda_0 = 570\,\text{nm}$ for optical bandwidth filtering before it hits the detector. The interference filter and the PMT are installed in a 2 inch tube system from Thorlabs, to suppress any external light. To exchange the ND filters for the different combinations, a

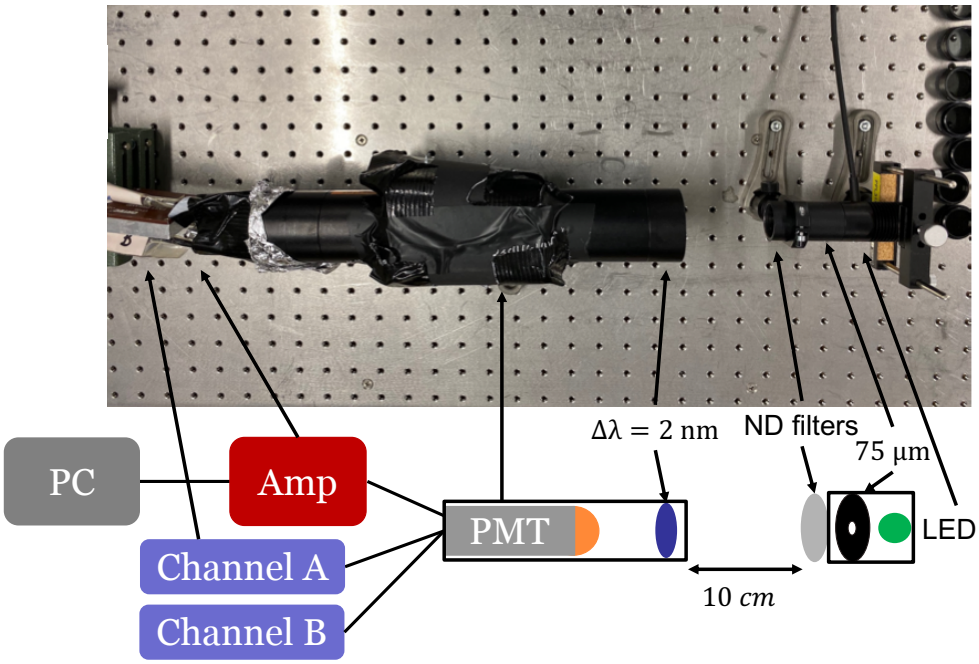

Figure 4.1: Upper: picture of the setup. Lower: schematic layout of the measurement setup. An LED with the center wavelength of 570 nm is placed in front of a FlashCam PMT. A 75 µm pinhole, various combinations of neutral-density filters and an interference filter of 2 nm were installed in between. The PMT signal is lead to an amplifier and to the computer. The PMT is connected to a voltage supply via two channels and to reduce any stray light from the outside, the PMT was wrapped in black cardboard and sealed with black duck tape.

distance of 10 cm was kept between the ND filters and the entrance of the tube system with the interference filter and the PMT. The FlashCam PMT used for this measurement is connected to an amplifier by ORTEC, which intensifies the signal by 200. Unlike as for the first measurements in Berlin, the PMT is connected to a power supply via two channels, to counteract the saturation effects. Channel A, which can be set to 1500 V, supplies all dynodes and channel B, which can be set to 500 V, only supplies the last two dynodes. The power supply used in this setup is the 660 Dual 5kV Bias Supply from ORTEC. For these measurements, a voltage of 1150 V for channel A and 500 V for channel B was chosen.
The intensified PMT signal is lead to a computer to record all measurement results for further analysis.
To reduce any incoming light, black cardboard was wrapped around the PMT tube, which was sealed with black duck tape. The distance between ND filters and the interference filter was also covered with black cardboard when measuring.

Table 4.1: Neutral-density filter combinations used to reduce the incoming light. The combination number, the filter combination and their measured transmission value are listed. The combination numbers marked in blue were used in the high rate measurements.

Combination number	ND filter combination	Measured transmission
03	20+10+6	0.0001
06	20+13+1	0.0003
09	20+10+1	0.0005
11	20+10	0.0007
13	20+6+1	0.0012
15	20+5+2	0.0014
17	20+5+1	0.0016
19	20+5	0.0019
20	20+2+1	0.0033
22	13+10+1	0.0042
24	20+2	0.004
26	13+10	0.005
27	20	0.0062
29	10+6+5	0.0089
32	13+6	0.0122
34	13+5	0.0163
36	10+6+1	0.022
37	10+5+2	0.0226
40	10+5+1	0.0293
42	10+5	0.0365
47	6+5+1	0.0668
48	10+2	0.0717
49	10+1	0.0897
53	6+2	0.1637
56	5+2	0.2277
60	2+1	0.5407

4.3 First Rate Measurements

The measurements were carried out for 26 combinations of the ND filters with transmissions listed in Table 4.1. The LED was set to a voltage of 2.5 V and a voltage range of ±100 mV was set in the analysis program "SBench", which the signal and waveforms were recorded with.
In Figure 4.2 a section of an 80 µs long obtained waveform for combination 32, meaning low rate, is shown. The plot presents the time in µs on the x-axis, which ranges from 8.0 to 8.5 µs. The region was chosen to illustrate the waveform baseline including photon pulses. The left y-axis shows the received amplitude of the signal in ADC counts and the right y-axis the amplitude converted to mV. From the graphic one can see that the baseline displays some electronic noise and a slight offset towards negative values. The offset can also be determined by calculating the mean of all the amplitudes in the waveform, which results in $-1.71\,\mathrm{ADC} = -1.34\,\mathrm{mV}$. A recorded waveform for combination 49, which corresponds to a higher rate than the one received with for combination 32, is shown in Figure 4.3. The baseline in this waveform also boasts noise with a similar offset to negative values. When calculating the mean, an offset of $-1.78\,\mathrm{ADC} = -1.40\,\mathrm{mV}$ is obtained. The proximity of both means is not of statistical nature. When calculating the mean of the low rate measurement 10 times for different, but equally long, sections of the waveform, the average results in $-1.707\,\mathrm{ADC} = -1.344\,\mathrm{mV}$. The error of this value is in this case negligible, since it is so small and the difference to the mean of the high rate measurement substantially bigger. In Figure 4.4, the mean of each obtained waveform is plotted against the transmission value. No pattern can be detected for increasing rates.
The corresponding pulse height histogram is shown in Figure 4.5. The histogram is produced by analyzing the waveform data with a peak finding python program. The program takes every bin data point and defines it as a minimum if the two neighboring bins have a higher value than the regarded bin itself. The minima are considered as peaks and their amplitude is collected. The histogram shows the count rate of peaks with a certain amplitude in respect to this amplitude, also pulse height. Around the pulse height of 0, one can see the pedestal peak, which corresponds to the electrical noise on the baseline, meaning all the minima with small amplitudes in the waveform. The other peak corresponds to the photon peak. The histogram shows that the pedestal peak shifts to positive values for higher transmissions, meaning higher rates, which also occurred in the first measurements in Berlin. The photon peak shifts to smaller negative values for increasing transmission values and overlaps with the pedestal peak at the highest transmissions, leading to the assumption that the saturation effects have not been solved yet. This performance is still rather unexpected and will be discussed later in this section.

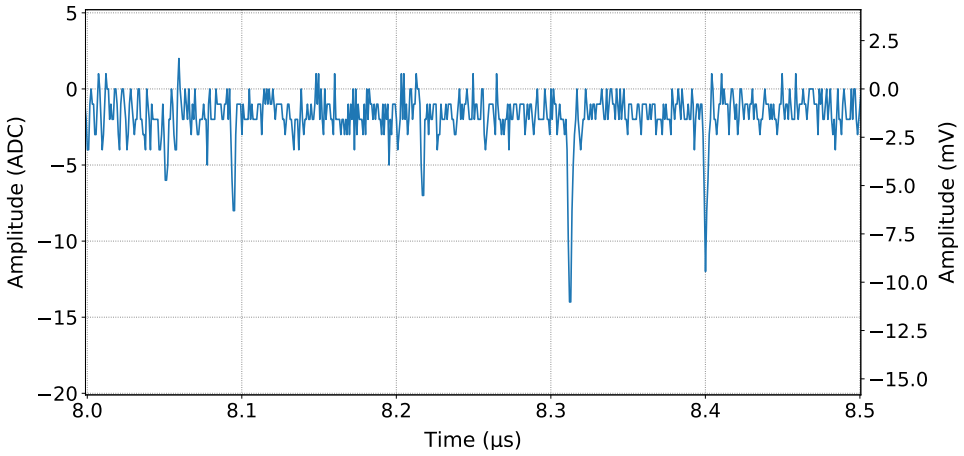

Figure 4.2: A section of the waveform of a FlashCam PMT for combination 32 with a transmission of 0.0122, corresponding to 10 MHz, with LED set at 2.5 V, is shown. The mean lies at $-1.71\,\mathrm{ADC} = -1.34\,\mathrm{mV}$.

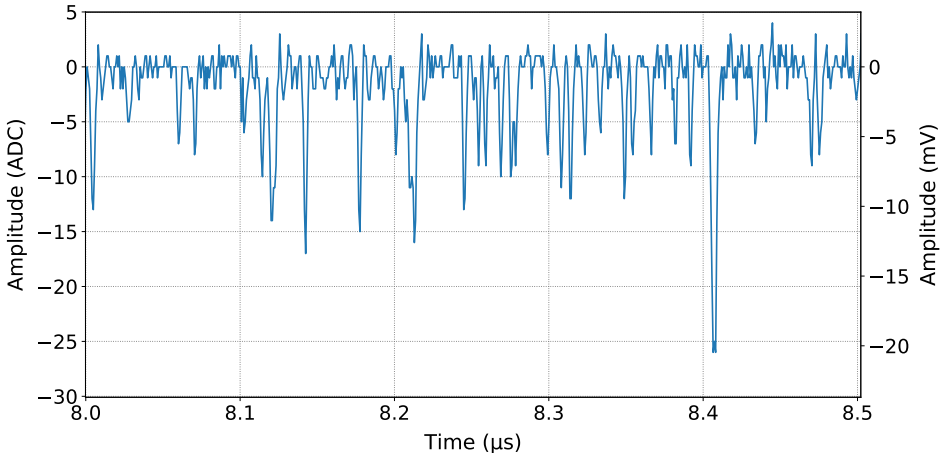

Figure 4.3: A section of the waveform of a FlashCam PMT for combination 49 with a transmission of 0.0897, corresponding to 60 MHz, with LED set at 2.5 V, is shown. The mean lies at $-1.78\,\mathrm{ADC} = -1.40\,\mathrm{mV}$.

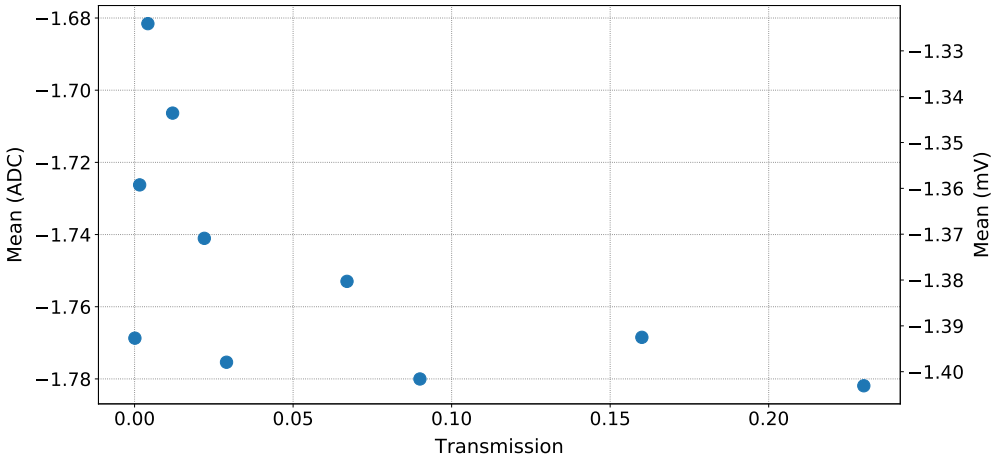

Figure 4.4: The mean of each waveform is plotted against the corresponding transmission value.

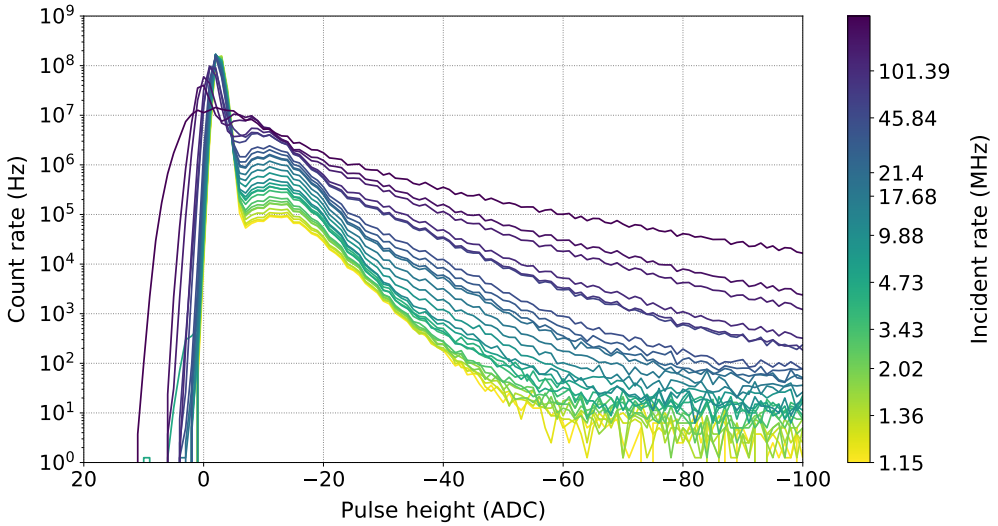

Figure 4.5: The pulse height histograms for a FlashCam PMT for different rates and LED setting of 2.5 V is shown. The pedestal peak of the noise and the photon peak move towards positive values until they completely overlap for high rates.

The estimated incident rate, which is written next to the color bar of the histogram, is calculated by applying a Gaussian distribution of the following form to the photon peak:

$$f(x) = a \cdot \exp\left(-\frac{(x-\mu)^2}{2\sigma^2}\right) \tag{4.1}$$

Here, σ corresponds to the standard deviation and μ to the mean value. Since the electron multiplication at the single dynodes is Poisson distributed, adding them up for all dynodes results in a good approximation of a Gaussian distribution [25]. The fit ranges from the minimum between pedestal and photon peak, which is adjusted for each curve, with no limit to high negative pulse heights. This limit was chosen in order to eliminate as much of the pedestal peak as possible but also to include as much of the photon peak as possible. An example is shown in Figure 4.6, where the histogram for combination 32, corresponding to 10 MHz, and the applied Gaussian fit are plotted. The y-axis was not plotted logarithmically, as in the other histograms, to show the alignment between data and fit. This calculation doesn't work for the highest transmission values, since the photon peak and the pedestal peak overlap, due to multi photon events. The form of the photon peak does not resemble the form of a Gaussian distribution anymore, because the tail of the fit and the real data do not correspond. This is the reason why the incident rate written next to the histogram only goes until 101.39 MHz, combination 53, and not all the way to the top of the color bar. The incident rate was then obtained by integrating the Gaussian fit and resulted in achieving the graph in Figure 4.7, which presents the obtained rate with respect to the transmission.
As mentioned above, μ in Equation 4.1 stands for the mean value of the Gaussian distribution. It also represents the mean pulse height at the corresponding rate. In Figure 4.8, the mean value of the photon peak in ADC counts and mV is plotted against the calculated rate. It shows again that the absolute value of the mean decreases for higher rates.

From the assumed incident rates in Figure 4.5, one can gather that they are too low in comparison to the 200-500 MHz which are expected at the H.E.S.S. telescopes for the brightest stars. In order to reach higher rates than 100 MHz, the LED voltage was increased to 2.7 V. The applied PMT voltage stayed at 1150 V for channel A and 500 V for channel B. For this measurement, only a few ND filter combinations were used, which are marked blue in Table 4.1. The same procedure as for the low rate measurements was done again and the obtained pulse height histogram is shown in Figure 4.9. It presents the count rate against the pulse height.

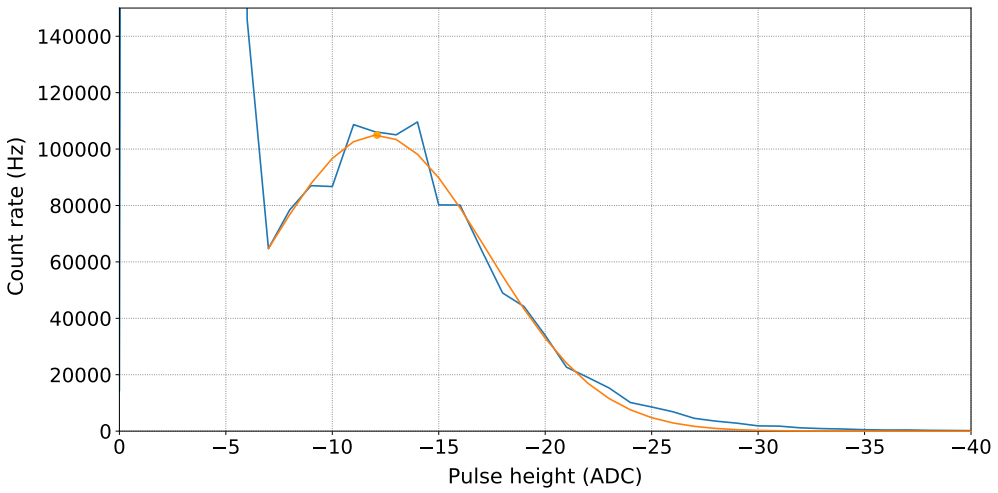

Figure 4.6: The pulse height histogram for a FlashCam PMT for 10 MHz and the applied Gaussian fit is shown. Both axes are plotted linearly, to show the accordance between data and fit.

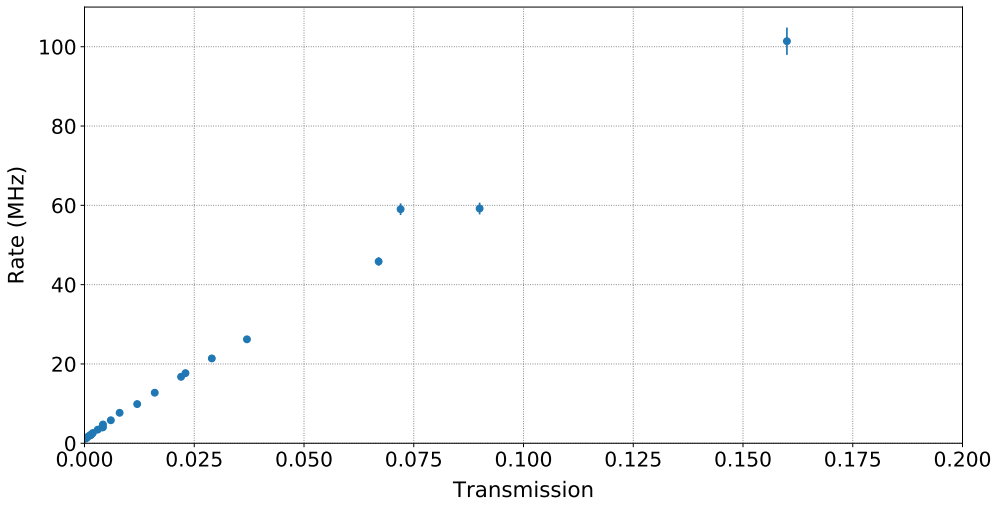

Figure 4.7: The determined rate via the Gaussian fit for the histogram in Figure 4.5 is shown with respect to the transmission up to combination number 53 with transmission 0.1637 and 101.39 MHz.

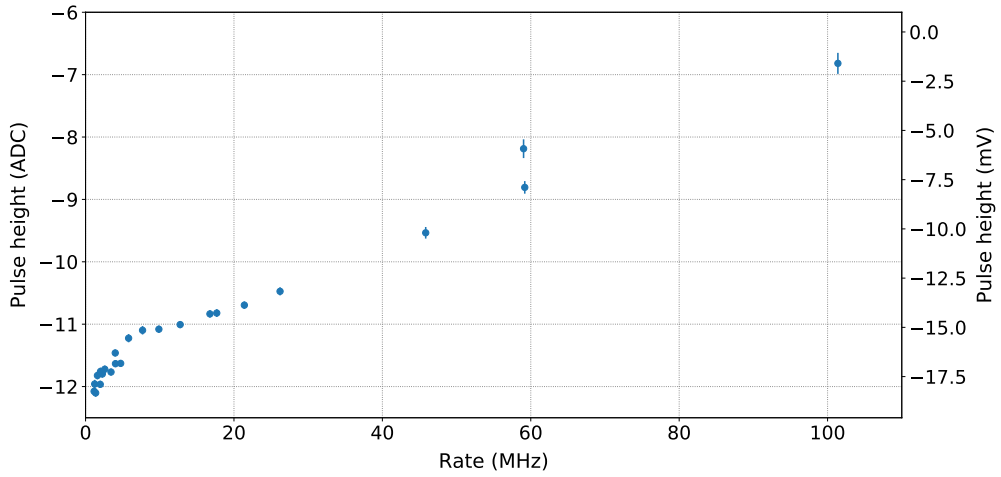

Figure 4.8: The mean of the Gaussian fit, the mean pulse height, with respect to the determined rates is shown. The absolute value of the mean decreases with increasing rate.

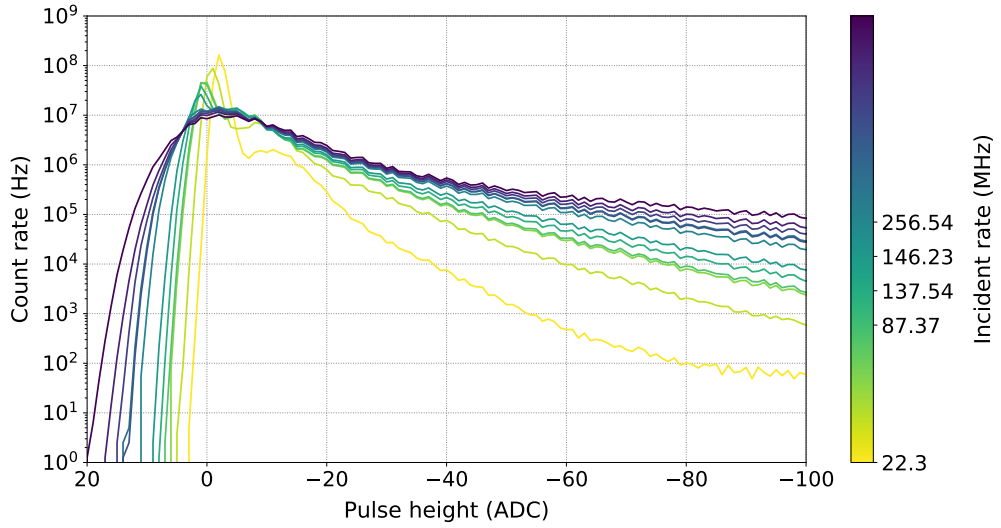

Figure 4.9: The pulse height histograms for a FlashCam PMT for different rates and LED setting of 2.7 V is shown. The pedestal peak of the noise and the photon peak move towards positive values until they overlap for high rates.

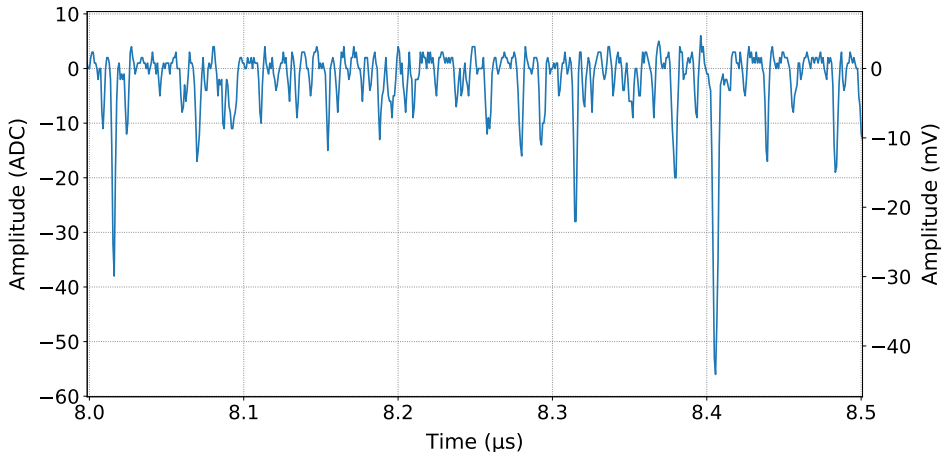

Figure 4.10: A section of the waveform of a FlashCam PMT for combination 15 with a transmission of 0.0014, corresponding to 150 MHz, with LED setting at 2.7 V, is shown. The mean lies at -1.79 ADC $= -1.41$ mV.

The curves show the same behavior as in Figure 4.5, where the pedestal peak and the photon peak move towards positive values and overlap at high rates. The calculated incident rate via applying the Gaussian distribution to the photon peak is listed next to the color bar. Since not all ND filter combinations were used, there is a gap between the first and second measured incident rate. It is evident from the figure that the fit does not work for high rates, since the photon peak does not resemble the shape of a Gaussian distribution anymore. In this case, the incident rate calculated with this method reaches 256.54 MHz.

Concerning the waveforms, the mean ADC value of the waveform doesn't change for low and high rates, as mentioned before and shown in Figure 4.4. Comparing a waveform of a low rate measurement of 10 MHz with a waveform of a high rate measurement of 150 MHz, as done in Figure 4.2 and Figure 4.10, it is apparent that the mean of both data is similar, with -1.71 ADC $= -1.34$ mV for 10 MHz and -1.79 ADC $= -1.41$ mV for 150 MHz measurement. This behavior and the fact that the pedestal peak and the photon peak move towards positive values is rather unexpected, since the assumption stands that with increasing rate the pulse height and the amount of photons, received at the PMT, increases. Due to the larger number of photons, single photon pulses might overlap in the waveform leading to higher absolute values for the pulse heights. Therefore, the mean of the waveform and the photon peak in the histogram should shift to larger negative values. This suggests that the saturation effects have not been solved by applying a new base to the PMT with two voltage channels instead of one. The pedestal peak is expected to stay around zero pulse height for low rates, since the noise peaks are always very

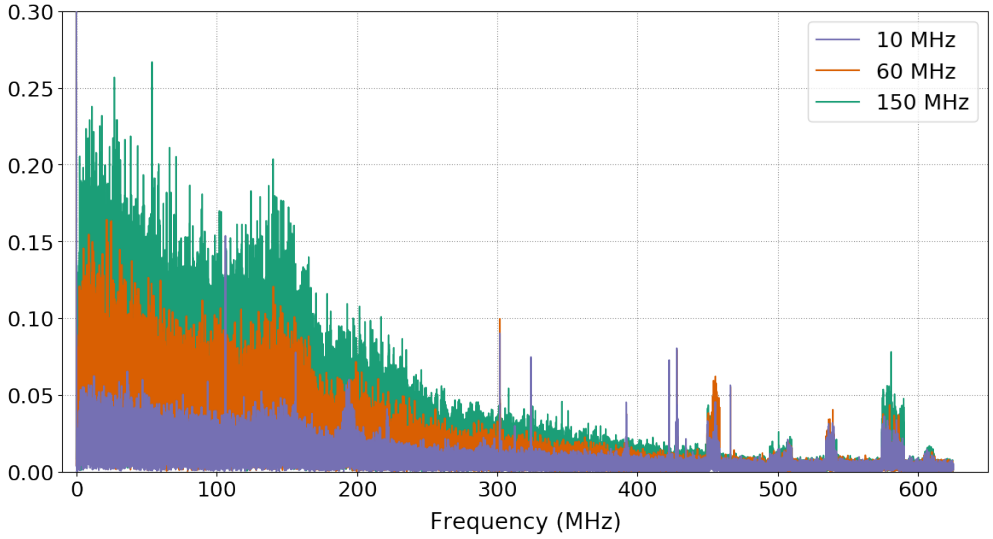

Figure 4.11: The FFTs of the waveforms for 10 MHz (blue), 60 MHz (orange) and 150 MHz (green), shown in Figure 4.2, Figure 4.3 and Figure 4.10, respectively, are arranged in one plot.

small and do not increase their pulse height. For high rates the count rate within the pedestal peak should decrease, since there are many photon pulses overlapping and exceeding the noise.

4.4 Waveform Simulations

Before simulating waveforms, the electric noise on the baseline of the waveforms was further investigated by performing Fourier transformations (FFT) of the waveforms for photon rates of 10 MHz, 60 MHz and 150 MHz, shown in Figure 4.2, Figure 4.3 and Figure 4.10, respectively. For a better overview, all FFTs are displayed in one plot in Figure 4.11. The x-axis represents the frequency and the y-axis is related to the strength of the frequency. The left part of the FFTs, which decreases towards higher frequencies, comes from the photon pulses. This is clarified later in this section. The peaks which can be found at frequencies higher than 300 MHz might stem from mobile services, weather radio services or space research radio services [26].

To further investigate the behavior of the baseline and photon peak, waveforms for different rates were simulated. First, a baseline of zeros with the same amount of 100 000 data points as the real data was created. Each data point resembles a time

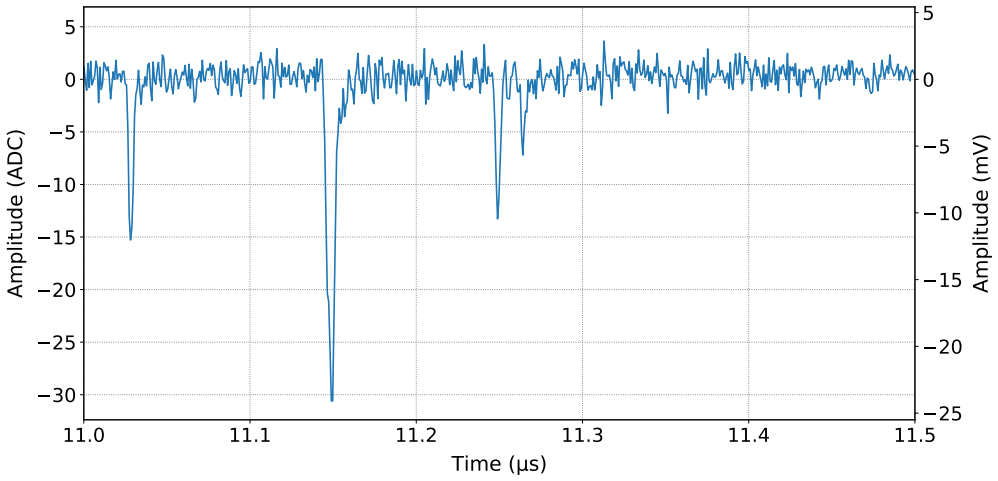

Figure 4.12: A section of a simulated waveform for 10 MHz is shown. The mean lies at $-0.03\,\mathrm{ADC} = -0.02\,\mathrm{mV}$.

bin of 0.8 ns, leading to a 80 µs long file. Then, photons are added randomly to the baseline. The shape of the added photons was achieved via a photon pulse shape template. The template was obtained by collecting the photon pulse shapes of a waveform of a reasonable rate (e.g. 10 MHz) and creating an average pulse shape out of the recorded ones. Different photon rates are adjusted within the simulation. Random Gaussian noise was also added to the baseline with $\mu = 0.4$ and $\sigma = 1.0$ to simulate the real measurement conditions as well as possible. Sections of simulated waveforms for 10 MHz and for 150 MHz are shown in Figure 4.12 and Figure 4.13. As expected and explained in the section beforehand, the waveform for 150 MHz shows a mean shift towards negative values because of the increased overlapping of photon pulses decreasing the mean. The waveform mean lies at $-6.08\,\mathrm{ADC} = -4.97\,\mathrm{mV}$. The waveform for 10 MHz on the other hand only has a small baseline shift due to the little amount of pulses. Its mean lies at $-0.03\,\mathrm{ADC} = -0.02\,\mathrm{mV}$.

With these considerations, the behavior of the real data described in section 4.3 seems inconsistent with the simulations. This results in the conclusion that a gain drop of the PMT is involved, meaning that the photon pulses saturate for high rates. The overall gain of the setup system is composed of the gain of the PMT and the gain of the amplifier. It can be assumed that the gain of the PMT decreases with increasing rate, because the last dynodes in the PMT can't recharge fast enough, leading to saturation of the pulses. Additionally, the ORTEC amplifier of 200, which is AC coupled, adds a baseline offset towards positive values when the mean of the waveform shifts to negative values, in order to compensate for this, since it is set to always return a similar mean. Furthermore, the amplifier only intensifies negative values, which means that for high rates, when the pulse heights

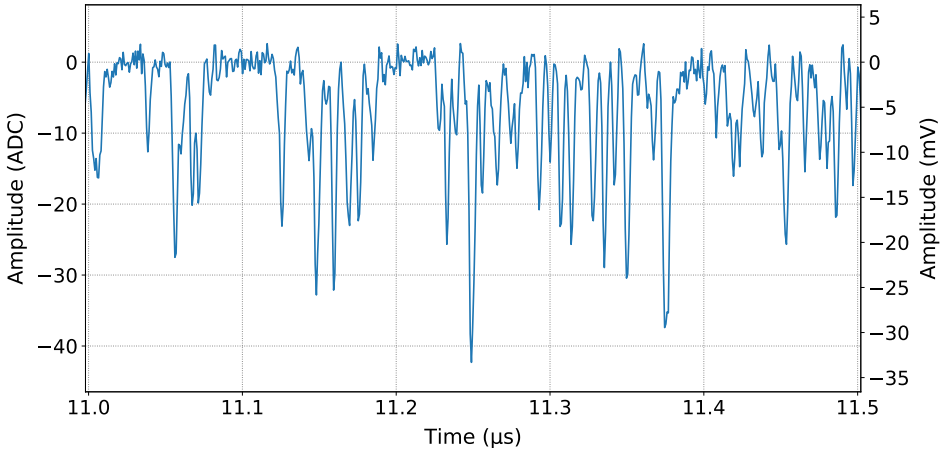

Figure 4.13: A section of a simulated waveform for 150 MHz is shown. The mean lies at $-6.08\,\mathrm{ADC} = -4.97\,\mathrm{mV}$.

are highly negative but an offset is created, saturation occurs.
The solution was using a new amplifier by FAST which is DC coupled and doesn't have the mentioned properties.

The noise mentioned in the section beforehand on the baseline of the waveforms is also investigated with the simulated data. FFTs of the simulated waveforms for 10 MHz and 150 MHz in Figure 4.12 and Figure 4.13 are shown in Figure 4.14. Since there are no extra oscillations considered in the simulations except for photon pulses and random Gaussian noise, the plot proves that the left part, which decreases with higher frequencies and is also present in the real data, stems from the photon pulses. No peaks at higher frequencies can be seen, meaning the peaks at high frequencies found in Figure 4.11 come from external signals.

The pulse height histograms of the simulations were also examined and compared to the real data. In Figure 4.15, three histograms of different rate simulations are shown. The blue one resembles 10 MHz, the orange one 150 MHz and the green one 500 MHz. The tale of the histograms gets longer with increasing rate because the amount of single photon pulses increases making them overlap in the waveform leading to higher absolute values for the pulse heights. The pedestal and the photon peak shift to the right towards more negative values, which is not the case when looking at the real data in Figure 4.5. This indicates additionally that a solution for the measurements is necessary. What can also be concluded is that the photon peak of the histogram does not resemble a Gaussian distribution anymore at 150 MHz, meaning a different method has to be developed for photon rate measurements at high flux.

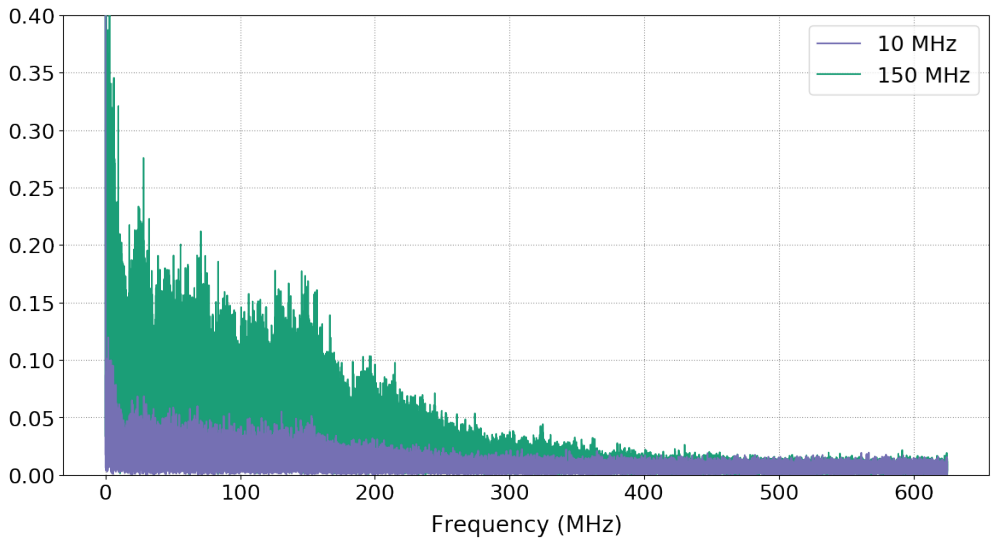

Figure 4.14: FFT of the simulated waveforms for 10 MHz (blue) and 150 MHz (green), shown in Figure 4.12 and Figure 4.13, are compiled in one plot.

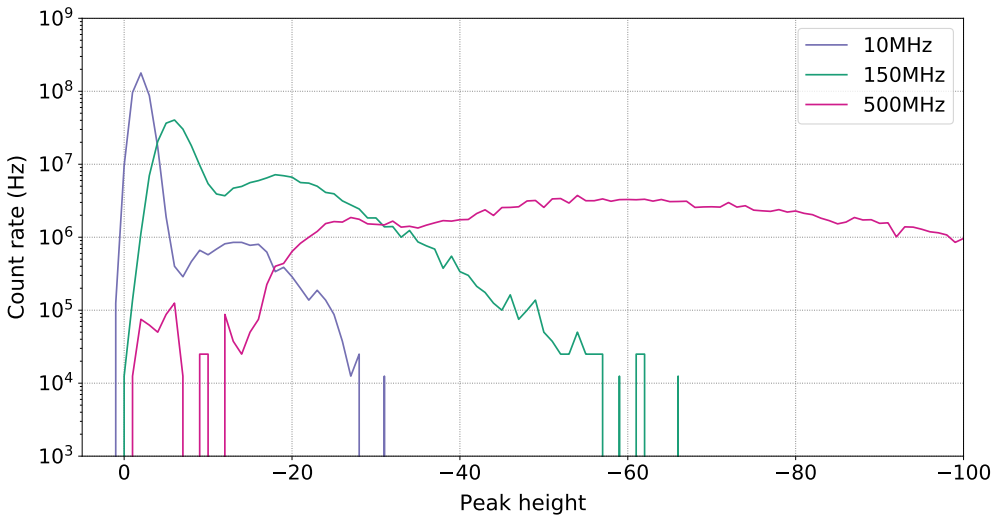

Figure 4.15: Pulse height histograms of simulated measurements with rates of 10 (blue), 150 (green) and 500 MHz (pink).

4.5 Second Rate Measurements

New measurements with an LED of 465 nm were taken, since the quantum efficiency of the PMT is higher in the blue wavelength range than in the green one. The LED was set to a voltage of 2.5 V and a voltage of 1100 V for channel A and 500 V for channel B was applied to the PMT. The new amplifier by FAST with amplification factor 200 was installed and a voltage range of ± 200 mV was set in the analysis program "SBench", with which the signal and waveforms were recorded. The obtained waveforms are illustrated in Figure 4.16 and Figure 4.17. The waveform for 10 MHz, which was calculated via the pulse height histogram, only has a small baseline shift towards positive values, which results from the noise peaks exceeding the few photon pulses. Its mean lies at $0.61\,\mathrm{ADC} = 0.96\,\mathrm{mV}$. Whereas for a rate of 150 MHz, the mean lies at $-13.06\,\mathrm{ADC} = -20.57\,\mathrm{mV}$.

The obtained pulse height histogram, count rate against pulse height, is shown in Figure 4.18 and it reflects the behavior of the simulated histograms in Figure 4.15. The photon peak moves to higher pulse heights with increasing rate. The incident rate next to the color bar is determined by applying and integrating a Gaussian distribution to the photon peak. Likewise to the previous histograms, the Gaussian fit does not work for higher rates, which is why the highest calculated rate lies at 146.81 MHz. This conclusion was also made for the simulated data. Comparing the histograms in Figure 4.15 to the ones in Figure 4.18, those for 150 MHz look similar to one another, confirming the validity of the new measurement results.

In Figure 4.19, the FFTs of the waveforms for 10 MHz and 150 MHz, shown in Figure 4.16 and Figure 4.17, are plotted. No peaks at high frequencies can be found in this FFT plot, due to shielding with aluminium foil and grounding. To reduce the noise coming from external signals, such as TV and radio signals, the PMT and cables to the amplifier and voltage supply were wrapped in aluminium foil. Furthermore, the PMT was grounded to the optical table with copper tape. Altogether, this shields the PMT signal from external noise.

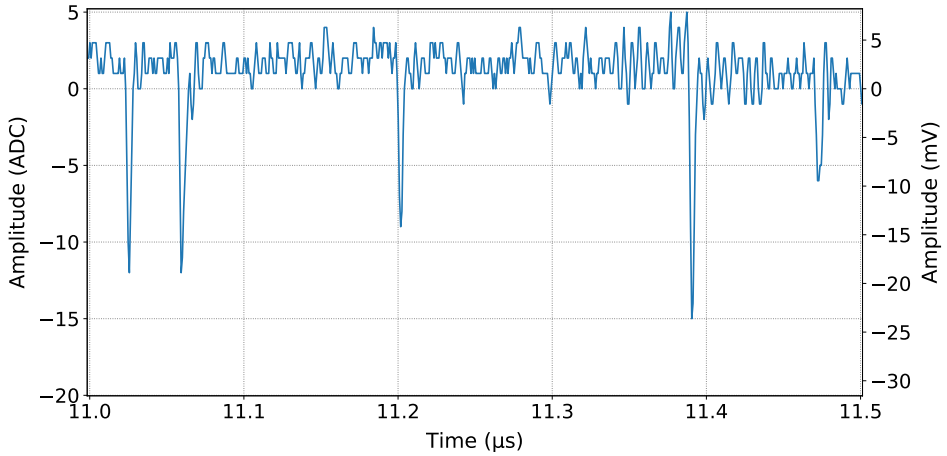

Figure 4.16: A section of the waveform of a FlashCam PMT with the new amplifier for combination 17 with a transmission of 0.0016, corresponding to 10 MHz, with LED set at 2.5 V, is shown. The mean lies at 0.61 ADC = 0.96 mV.

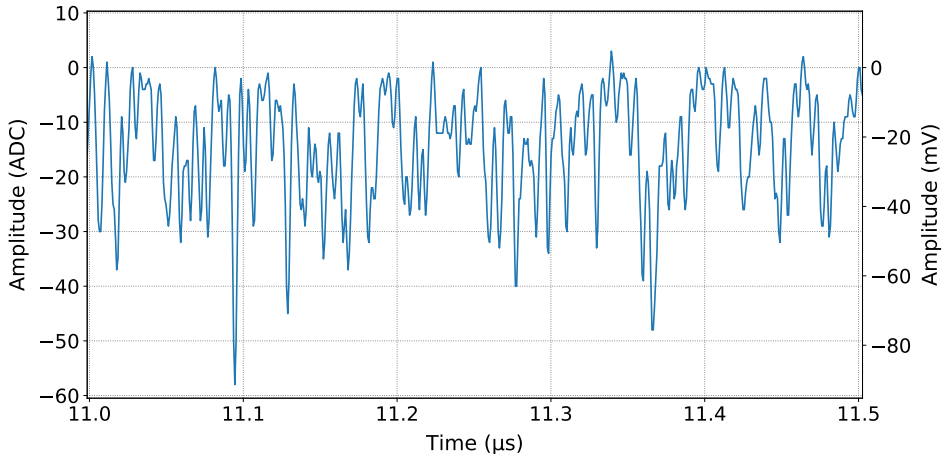

Figure 4.17: A section of the waveform of a FlashCam PMT with the new amplifier for combination 42 with a transmission of 0.0365, corresponding to 150 MHz, with LED set at 2.5 V, is shown. The mean lies at −13.06 ADC = −20.57 mV.

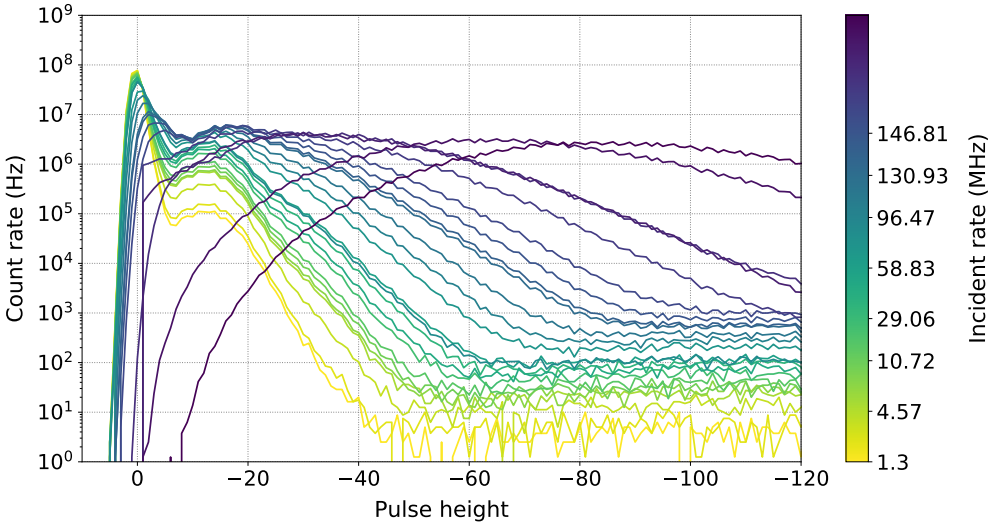

Figure 4.18: The pulse height histograms for a FlashCam PMT with the new amplifier for different rates and LED setting of 2.5 V is shown. The photon peak moves towards negative values and the count rate within the pedestal peak decreases until it overlaps with the photon peak.

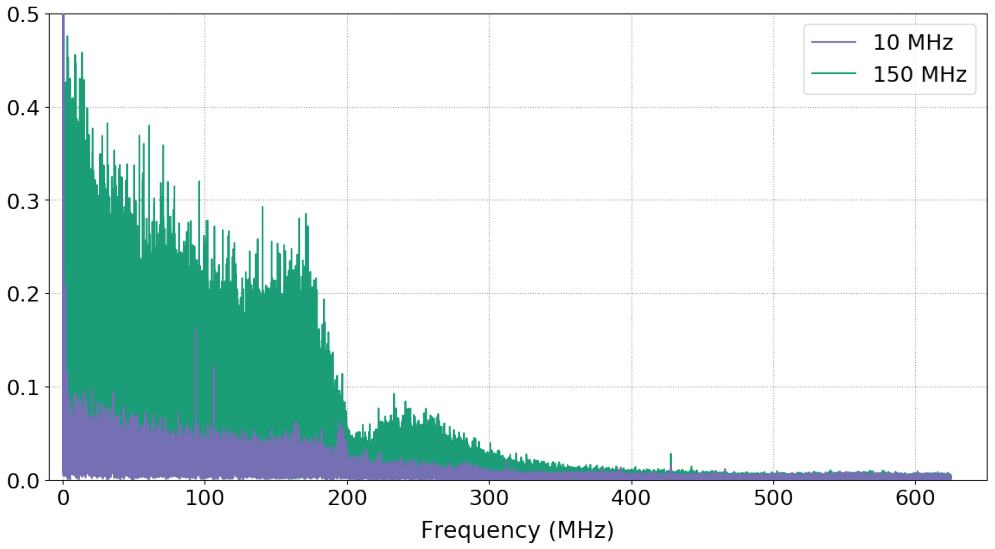

Figure 4.19: FFT of the waveforms for 10 MHz (blue) and 150 MHz (green), shown in Figure 4.16 and Figure 4.17, are compiled in one plot.

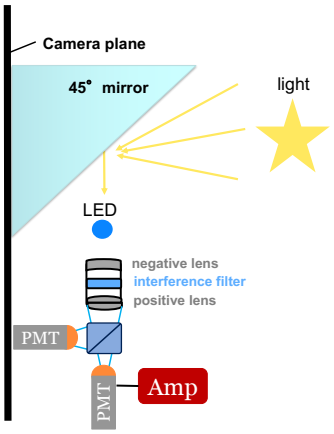

Figure 4.20: The Setup mounted on the MST consists of an LED, for reference measurement, installed in front of two FlashCam PMTs. 2-inch optics, negative lens (f = 7.5 cm), 2 nm interference filter, positive lens (f = 10 cm), for optical filtering are built in between LED and beamsplitter.

4.6 Measurement Berlin 2020

In February 2020, we took our correlation setup to the Medium-Sized Telescope (MST) prototype in Adlershof, Berlin. The setup, which is shown in Figure 4.20, consists of two FlashCam PMTs, a beam splitter, 2-inch optics and a 45 ° mirror, all mounted on the camera plane of the MST. The signal of the PMTs is led to the computer via amplifiers with amplification factor 200. The LED can be installed directly in front of the optics for reference measurements, meaning measurements of systematics. The PMT setup is attached to a small optical table, which can be moved via small motors. The angles of the 45 ° mirror can also be changed via small motors in order to bring the reflected starlight in alignment with the entrance window of the lenses. Additionally, the setup was shielded with aluminium foil and grounded, in order to avoid electric noise.

Due to disadvantageous observation conditions, no stars were visible long enough through the clouds to take a correlation measurement. Instead, a reference correlation measurement with the LED directly in front of the optics was carried out to investigate what effects the setup and the telescope motors and the surroundings at the telescope have. The result is shown in Figure 4.21. The upper plot shows the $g^{(2)}$ function with x-axis as number of time bins of 800 ps. The lower plot shows the corresponding FFT. Due to an installed cable delay, the correlation signal should be around the 95th time bin in the upper plot. But it cannot be seen because of unwanted oscillations. As mentioned before, calculating the FFT is a reliable method to check for any noise oscillations. Although a lot of aluminium foil was

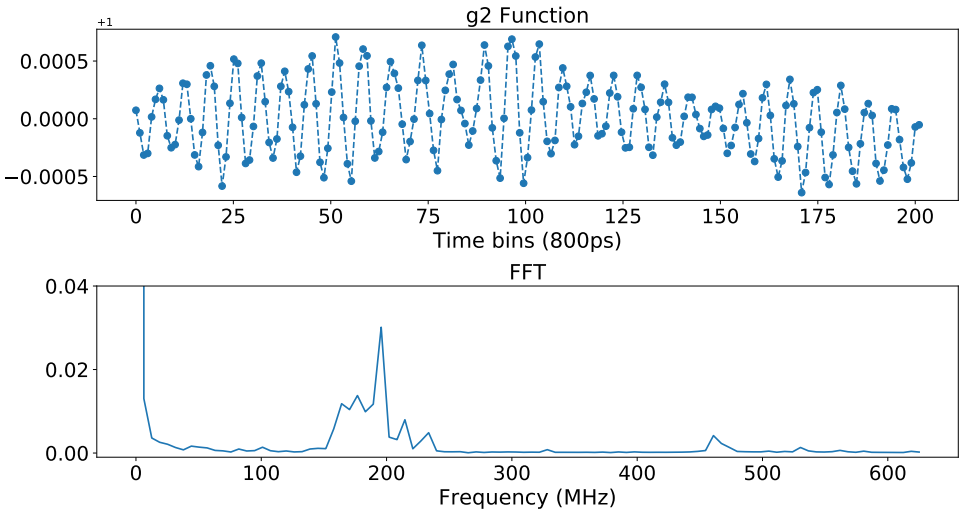

Figure 4.21: Upper plot: $g^{(2)}$ function. lower plot: FFT showing noise oscillations around 200 MHz from TV and radio stations.

used as shielding against electric noise, oscillations exist around 200 MHz, which come from TV and radio stations in the area.
Due to the fact that internal amplification of the FlashCam PMT is not high enough, an amplifier with high amplification is used. The disadvantage is that the noise, which is captured by the PMT, is also amplified and outweighs the correlation signal in the measurement.
This led to the decision to carry out further measurements with the Hamamatsu PMT. It has a higher internal amplification, making it possible to use an amplifier with less amplification, meaning less noise, since it won't be amplified as much, and thus a more stable baseline.

Chapter 5

Systematic Waveform Investigations Using the Hamamatsu PMT

Contents

This chapter addresses the characterization for rate measurements of a Hamamatsu PMT. The characterization is based on several measurements conducted at different rates and their analysis via python programs like in chapter 4.
First, the advantages of the Hamamatsu PMT over the FlashCam PMT, as indicated in section 4.6, are described and the implications for the planned H.E.S.S. campaign. Secondly, rate measurements with a Hamamatsu PMT are introduced. As the expected rates at the H.E.S.S. telescopes exceed the rates determined via Gaussian distribution, a second version for determining higher rates was developed. The later introduced method via the mean of the waveform can be used successfully for even higher rates than the anticipated 500 MHz.

5.1 Rate Measurements

As mentioned in section 3.1 and section 4.6, the Hamamatsu PMT has several advantages over the FlashCam PMT for intensity interferometry measurements at the H.E.S.S. telescopes. Since it has a higher internal amplification, an amplifier with less amplification is necessary. For this purpose the amplifier by FAST with

amplification factor 200 was remodeled by Adrian Zink to achieve an amplification factor of only 10. This should have the effect that the noise, which is collected e.g. from TV, radio, weather and mobile stations, is less intensified, but the photon signals are amplified more via the PMT amplification itself, leading to a more stable baseline and better signal-to-noise. Furthermore, the Hamamatsu PMT has a higher gain, meaning more dynodes. Two HV channels are connected to the PMT as mentioned in section 3.1 but for simplicity, only the main voltage setting will be mentioned in the following.

The measurement setup remains unchanged compared to section 4.2, except for changing the FlashCam PMT for a Hamamatsu PMT and the amplifier with amplification factor 200 for the amplifier with amplification factor 10. Additionally, a different HV power supply by CAEN is installed.

The first measurements for low rates were carried out for the first 20 combinations, up to combination number 42, of the ND filters with transmissions listed in Table 4.1 in order not to exceed the PMT current limit of 100 µA. The LED was set to a voltage of 2.5 V and a voltage range of ±200 mV was set in the analysis program "SBench", with which the signal and waveforms were recorded. A main voltage of 900 V was applied to the PMT.
In Figure 5.1, a section of an obtained waveform for combination 06, corresponding to 10 MHz, is shown. The plot presents the time in µs on the x-axis, which ranges from 7.0 to 7.5 µs, to focus on the waveform baseline including photon pulses. The left y-axis shows the received amplitude of the signal in ADC counts and the right y-axis shows the amplitude converted to mV. In contrast to the baseline for the FlashCam PMT measurements, which showed noise oscillations, this baseline is very stable with no offset, making it easy to count the appearing photons via a peak finding python program. The mean of all the amplitudes in the waveform results in $-0.19\,\mathrm{ADC} = -0.30\,\mathrm{mV}$. A recorded waveform for combination 26, which corresponds to 100 MHz, is shown in Figure 5.2. The same x-axis region shows a lot more photons and the mean results in $-4.87\,\mathrm{ADC} = -7.66\,\mathrm{mV}$. As expected from the simulations in section 4.4, the mean for the higher rate shifts to negative values, because of the increased amount of photon pulses.
The pulse height histogram, shown in Figure 5.3, reflects the same behavior as in the simulations. The photon peak moves to higher negative pulse heights with increasing rates, meaning more overlapping photon pulses. For low rates the photon peak only shifts slowly, indicating that is it independent of the incident rate. This means that the absolute pulse height doesn't increase with increasing photon rate but because of multi photon events. The count rate of the pedestal peak decreases until it merges with the photon peak. The incident rate next to the color bar is determined by applying and integrating a Gaussian distribution to the photon peak.

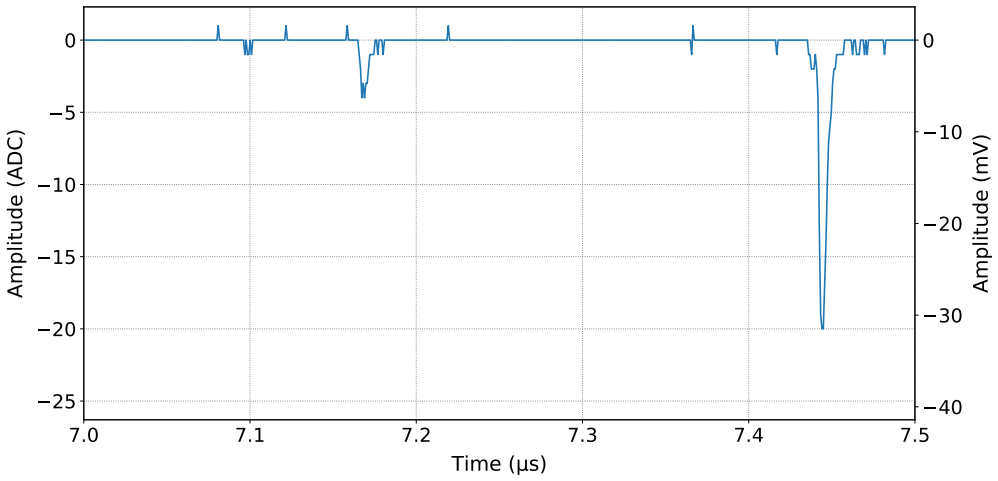

Figure 5.1: A section of the waveform of a Hamamatsu PMT for combination 06 with a transmission of 0.0003, corresponding to 10 MHz, with LED set at 2.5 V and PMT main voltage at 900 V, is shown. The mean lies at $-0.19\,\mathrm{ADC} = -0.30\,\mathrm{mV}$.

Similar to the previous histograms, the Gaussian fit does not work for higher rates, which is why the highest calculated rate lies at 110.34 MHz.
Since the maximal determined rate is only 110.34 MHz, which is too low in comparison to the expected rate at the H.E.S.S. telescopes, new measurements for higher rates were done, similar to those with the FlashCam PMT in section 4.3. The LED voltage was left to 2.5 V, but the PMT main voltage was decreased to 750 V. The measurement was carried out for all 26 ND filter combinations listed in Table 4.1. A section of a waveform, recorded with the analysis program "SBench", where the voltage range was set to ±200 mV, is shown in Figure 5.4. The transmission for the installed ND filters was 0.5407 (combination 60), corresponding to a very high rate. The mean of this waveform lies at $-33.45\,\mathrm{ADC} = -52.68\,\mathrm{mV}$, since the overlapping photon pulses with their increased absolute pulse height pull down the mean towards negative values. These overlapping single photon pulses make it hard to distinguish them and create a useful pulse height histogram.
Looking at the pulse height histogram in Figure 5.5, it is clear that determining the rate via Gaussian fit is no longer possible, since the form of the photon peak and the form of the Gaussian distribution don't match. Therefore, a different method has to be applied, which is described in the next section.

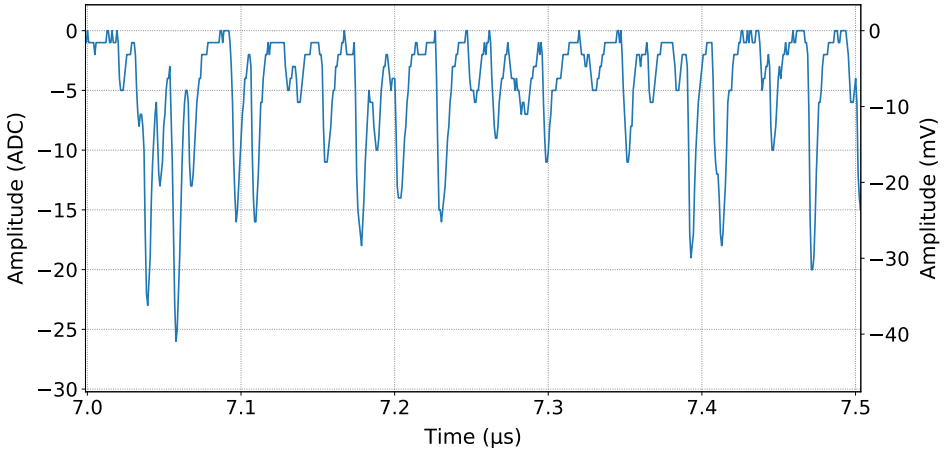

Figure 5.2: A section of the waveform of a Hamamatsu PMT for combination 26 with a transmission of 0.005, corresponding to 100 MHz, with LED set at 2.5 V and PMT main voltage at 900 V, is shown. The mean lies at -4.87 ADC $= -7.66$ mV.

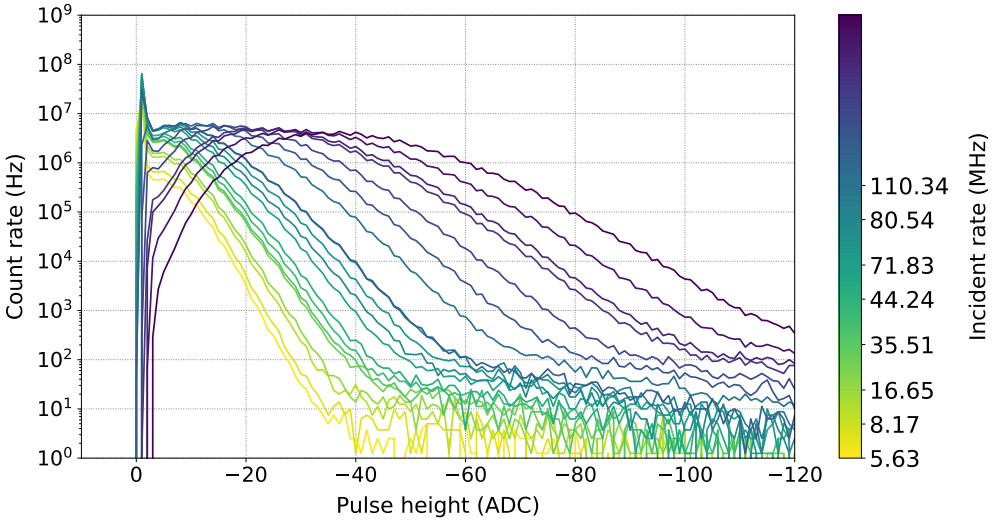

Figure 5.3: The pulse height histograms for a Hamamatsu PMT for different rates with LED setting of 2.5 V and PMT main voltage at 900 V is shown. The photon peak moves towards higher negative values with increasing rate.

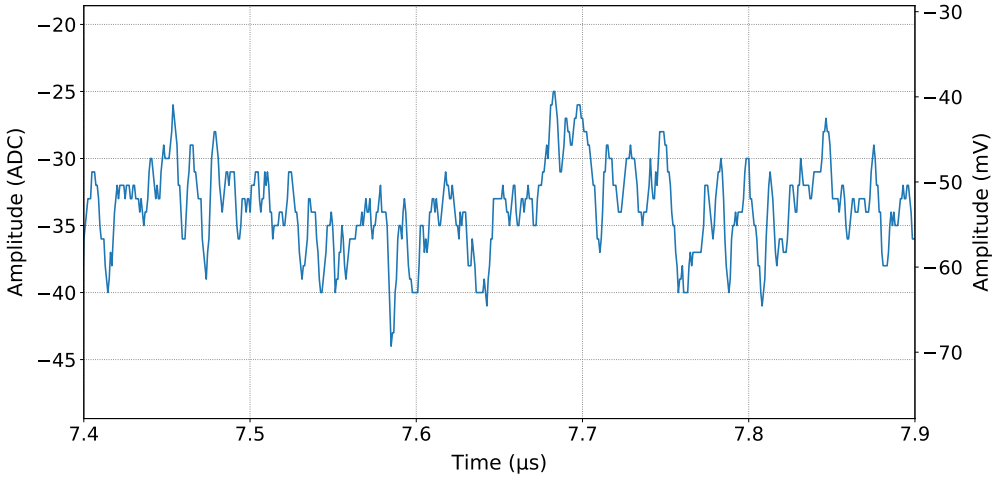

Figure 5.4: A section of the waveform of a Hamamatsu PMT for combination 60 with a transmission of 0.5407 with LED set at 2.5 V and main PMT voltage at 750 V is shown. The mean lies at $-33.45\,\mathrm{ADC} = -52.68\,\mathrm{mV}$.

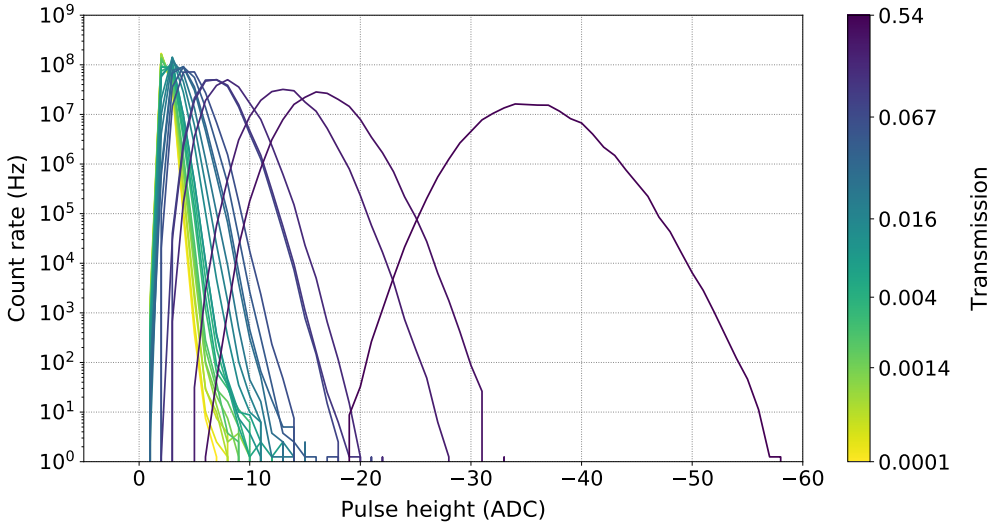

Figure 5.5: The pulse height histograms for a Hamamatsu PMT for different rates with a LED setting of 2.5 V and main voltage 750 V is shown.

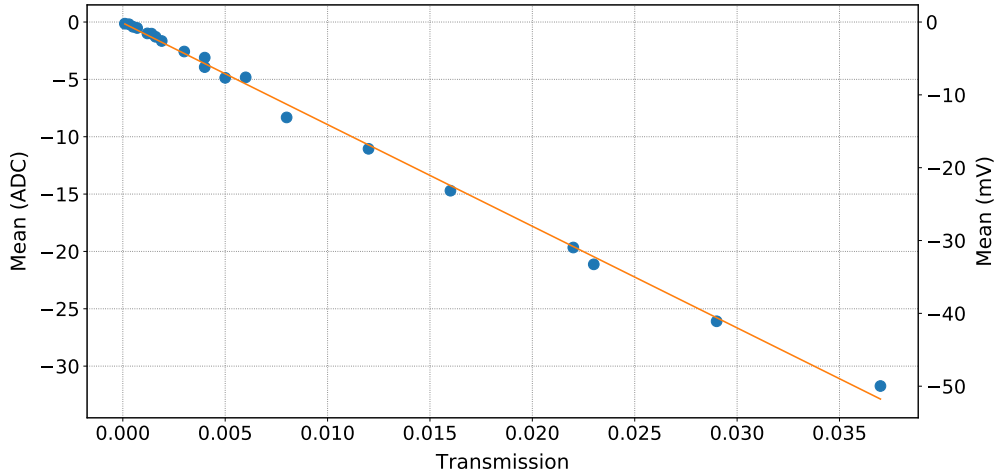

Figure 5.6: The mean of each waveform of the low rate measurement is plotted against the corresponding transmission value and a linear fit is applied (orange).

5.2 Determining Rate via Waveform Mean

This different method for determining the rate of a measurement is related to the mean of the waveform. For low rate measurements, it is possible to determine the rate by applying and integrating a Gaussian fit to the photon peak of the pulse height histogram, as done for the Hamamatsu PMT in section 5.1. For high rate measurements, this method cannot be applied anymore, since the shape of the photon peak of the histogram doesn't correspond to a Gaussian shape.

The first step is to investigate the mean of the waveforms of the low rate measurement further. In Figure 5.1 and Figure 5.2, two sections of an obtained waveform for 10 and 100 MHz are shown. The mean of all the amplitudes in the waveforms lies at $-0.19\,\mathrm{ADC} = -0.30\,\mathrm{mV}$ and $-4.87\,\mathrm{ADC} = -7.66\,\mathrm{mV}$, respectively. This calculation was done for all the 20 ND filter combinations measured and the result is plotted in Figure 5.6. From Table 4.1 one can gather that the transmission for the last measured combination number 42 is 0.0365. The plot shows the mean of the waveform in ADC or converted to mV against the transmission value for each measurement. As already determined, the mean decreases with increasing rate, since the growing amount of photon pulses pull it towards higher negative values. The graph also shows a linear relation between mean and transmission, which is marked by the applied linear fit in orange.

Plotting the mean against the determined rate via Gaussian fit from the histogram in Figure 5.3, which is only possible up to combination number 27 with a transmission of 0.0062 resulting in 110.34 MHz, no linear relation is visible in Figure 5.7.

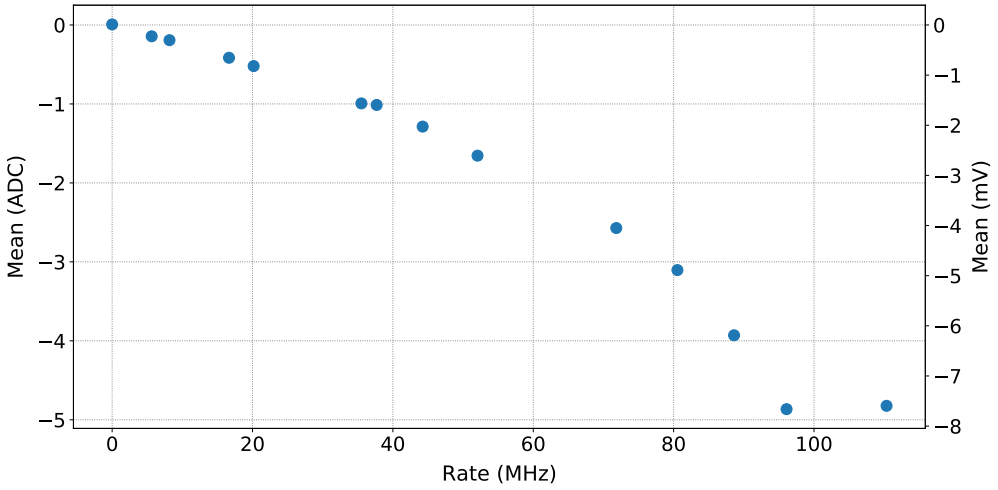

Figure 5.7: The mean of each waveform of the low rate measurement is plotted against the assumed rate determined via Gaussian fit from the pulse height histogram in Figure 5.3.

This also confirms that the method for determining the rate via Gaussian fit is not reliable for higher rates than approximately 60 MHz.
The next step is to establish the assumed rate via Gaussian fit against the transmission, which is shown in Figure 5.8 in blue with the first six data points in orange. The highest possible determined rate lies at 110.34 MHz for combination 27 with a transmission of 0.0062. The blue linear fit applied to all the data points doesn't reflect their path accurately, due to the fact that the higher rates are not reliable. This is the reason why the linear fit was only applied to very low rates, namely the first six data points plotted in orange. The data points leading up to a rate of 37.69 MHz for combination 15 with a transmission of 0.0014, were chosen. The orange linear fit of this section of the plot rate against transmission was plotted up to a transmission of 0.006, in order to compare it with the blue fit. The equation for the orange straight line is:

$$\mathrm{R} = 2.041 \cdot 10^4 \cdot \mathrm{T} + 3.287 \tag{5.1}$$

where R is the rate and T the transmission. Having evaluated a linear connection between transmission and rate, one can now convert the transmission values from Figure 5.6 into rates via this equation, which is done in Figure 5.9. Comparing this plot to Figure 5.6, it again shows a linear behavior, in contrast to Figure 5.7, where the rate was calculated via Gaussian distribution and no linear behavior can be seen.

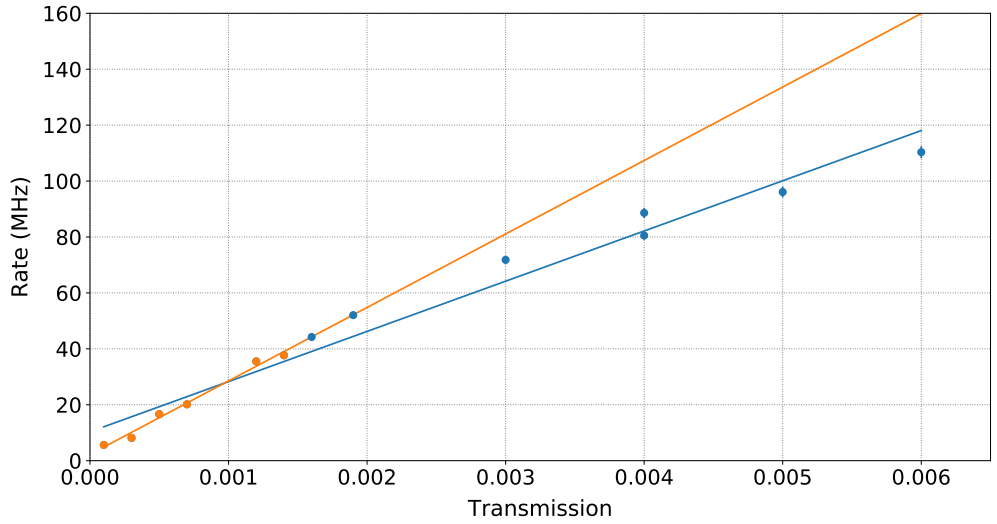

Figure 5.8: The determined rate via Gaussian distribution from the pulse height histogram in Figure 5.3 of the low rate measurement is plotted in blue and orange against the respective transmission value with applied linear fit in blue. The first six data points with low rates are marked in orange and a linear fit was also applied (orange).

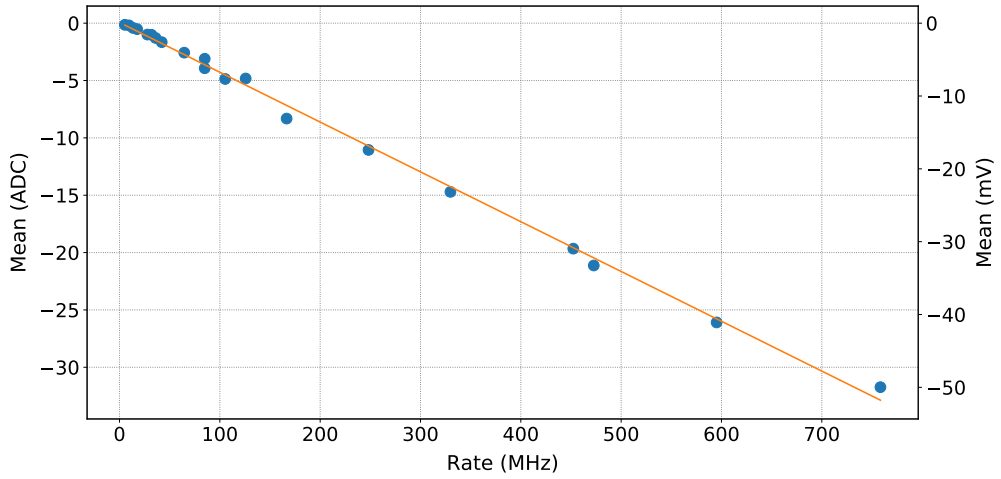

Figure 5.9: The mean of each waveform of the low rate measurement is plotted against the rate calculated via Equation 5.1 from Figure 5.8 and a linear is applied (orange).

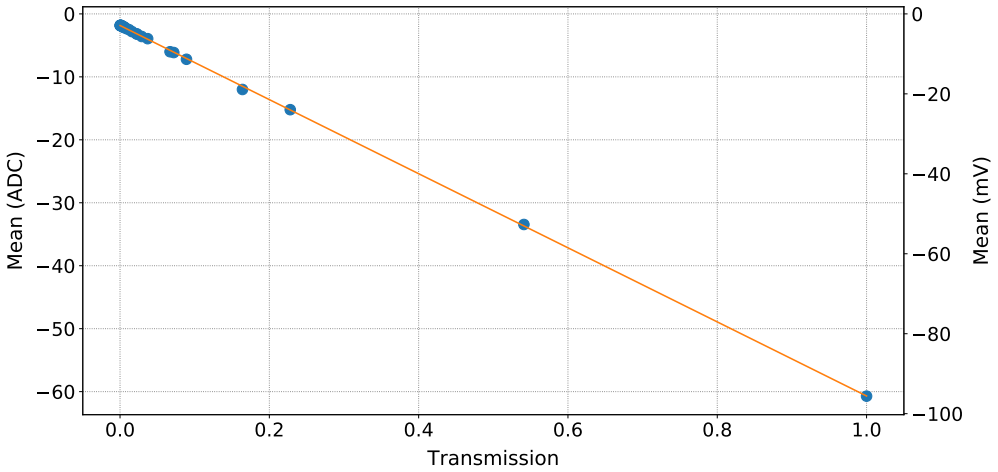

Figure 5.10: The mean of each waveform of the high rate measurement is plotted against its corresponding transmission value with applied linear fit (orange).

After establishing the linear relation between mean and transmission or rate for the low rate measurement, the same was done for the high rate measurement, where the LED voltage was left to 2.5 V and the PMT main voltage was decreased to 750 V in order to allow higher rates. The waveform for combination 60 with the highest transmission value of 0.5407, as already discussed earlier, is shown in Figure 5.4. The mean lies at $-33.45\,\mathrm{ADC} = -52.68\,\mathrm{mV}$. The mean of the other 25 ND filter combinations was also calculated and plotted against the transmission. This is illustrated in Figure 5.10 and shows a linear behavior. Since this is the case and the LED voltage was not increased, meaning the photon rate of the LED for the different ND combinations stayed the same as in the last measurement, one can take Equation 5.1 from the low rate measurement and convert the transmission into rate again, which results in the plot in Figure 5.11. For the waveform section, shown in Figure 5.4, this means a rate of 11 039 MHz was achieved, which is more than enough for having conditions similar to those at H.E.S.S. If now a measurement without known transmission value is taken, the mean of its waveform is calculated and its rate can be determined via the linear fit in Figure 5.11, which results in:

$$\mu = -0.002883 \cdot R - 1.834 \tag{5.2}$$

where μ is the mean of the waveform and R the rate. Inserting for e.g. the mean $-33.45\,\mathrm{ADC}$ in this equation, a rate of 11 172 MHz is achieved, which is very close to the result via Equation 5.1.

Summarizing the method for determining the rate, first a low rate measurement is taken and the rate is determined via fitting and integrating a Gaussian distribution

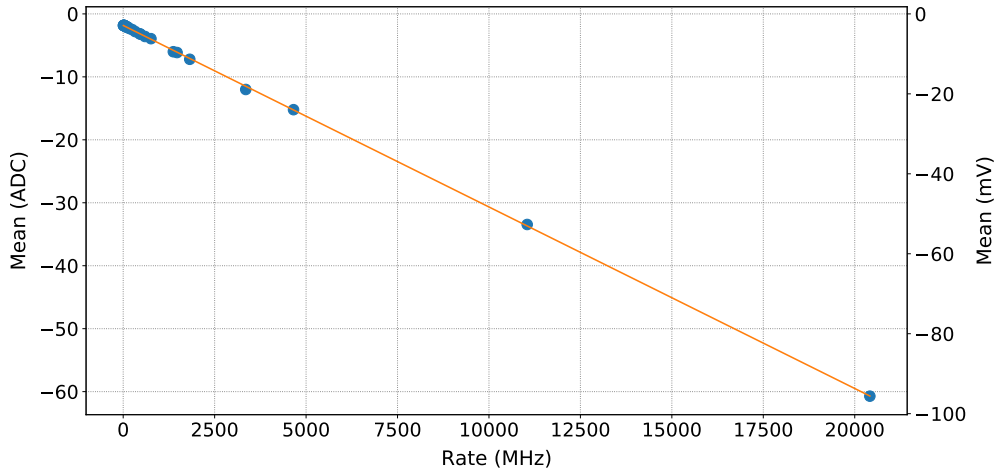

Figure 5.11: The mean of each waveform of the high rate measurement is plotted against the rate calculated via Equation 5.1 and a linear fit is applied (orange).

to the photon peak of the pulse height histogram. This rate is plotted against the transmission values of the measurement and a linear fit is applied to the lowest data points. The linear equation of the straight line is used for extrapolating. The next step is to calculate the mean of each waveform of the low rate measurement and plot it against the transmission values, which are then converted to rates via the extrapolation.
A second high rate measurement is taken where the rate cannot be calculated via Gaussian distribution of the pulse height histogram. The mean of each waveform is plotted against the transmission, which is converted to rate via the extrapolation. Then a linear fit is applied to the plot mean against rate and with the help of its linear equation, the rate of any measurement of the same PMT voltage can be calculated via its waveform mean. However, this means that such calibration curves would have to be determined for all possible PMT voltages.

Chapter 6

Hamamatsu PMT Calibration

Contents

This chapter addresses the calibration of the Hamamatsu PMT.
At first, the voltage calibration is discussed. The background for the measurements is described and the received knowledge will be of great usefulness for the planned H.E.S.S. campaign. The voltage calibration is based on several measurements conducted at different main voltages applied to the PMT but at the same rate and their analysis via python programs. Again, waveforms and photon pulse height histograms are observed. The photon pulse shape, which is specific for each type of PMT, also for the Hamamatsu PMT, is established .
Secondly, the correlation calibration is discussed. This section will focus on how a correlation measurement with previous voltage calibration will be carried out and analysed at the H.E.S.S. telescopes.

6.1 Voltage Calibration and Pulse Shape

The voltage calibration consists of measurements with the Hamamatsu PMT carried out for various main and booster voltages but for consistent rate. The goal is to learn more about the photon pulse height and the pulse shape and what effects different voltage settings have on them.

It was already established that the pulse height is independent of the incident rate but for high rates photons start to overlap creating multi photon peaks with higher pulse heights, which can be deduced from the pulse height histogram in section 5.1 in Figure 5.3. Now it is of interest how the pulse height behaves for different PMT voltages.
It is also important to know what the pulse shape of the Hamamatsu PMT looks like, e.g. for simulations for quantitative understanding of correlation measurements, and if it changes when applying different voltages to the PMT.

6.1.1 Voltage Calibration Measurements

The setup used for the voltage calibration is shown in Figure 6.1. It consists of an LED with a center wavelength of $\lambda = 465\,\text{nm}$. The ND filters with optical density number 20, 6 and 2 were inserted between the LED and the installed Hamamatsu PMT with the amplifier with amplification factor 10. Since neither the voltage applied to the LED nor the ND filters were changed, these measurements were taken at the same rate.
For the measurements the LED voltage was set to 2.2 V, since for low rates there are little photon pulses, which makes it easier to establish a pulse height histogram with single photon peak and to investigate the single photon pulse shape. The incident rate of about 1.0 MHz was calculated via the pulse height histograms and applied Gaussian distribution. The voltage range of $\pm 200\,\text{mV}$ was set in the analysis program "SBench", with which the signal and waveforms were recorded. The sampling rate in the mentioned program was also changed from a 0.8 ns sampling to a 1.6 ns sampling. The sampling rate refers to the time period between two taken data points in the waveforms. The first advantage is that only half the disk space is necessary for a measurement and it takes less time to transfer the data to the hard disk. This means that one hour measuring time results in about one hour of data, whereas beforehand, one hour of measuring time resulted in about 20 minutes of data. Table 6.1 lists all the used main voltages and the corresponding booster voltages. The range for the listed main voltages was chosen by examining each waveform and pulse heights at the same rate. Since the maximum applied main voltage is 1000 V and the pulse heights are too high for the set voltage range in the program, 900 V was chosen as a maximum. For lower main voltages than 750 V the gain is too low resulting in too small photon pulses to detect and analyse. For simplicity, only the main voltage will be mentioned when discussing the measurements.

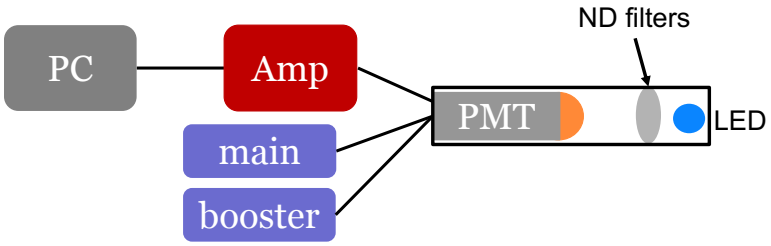

Figure 6.1: Schematic layout of the measurement setup. An LED with the wavelength of 465 nm is placed in front of a Hamamatsu PMT with ND filters number 20, 6 and 2 between. The PMT signal is lead to an amplifier and to the computer. The PMT is connected to a voltage supply via two channels and to reduce any stray light from the outside, the PMT, ND filter and LED are placed in a 2 inch tube system.

Table 6.1: Main and booster voltage used for the Hamamatsu PMT for the calibration measurements are listed.

Main voltage (V)	Booster voltage (V)
900	243
890	241
880	238
870	235
860	233
850	230
840	227
830	224
820	222
810	219
800	216
790	214
780	211
770	208
760	205
750	203

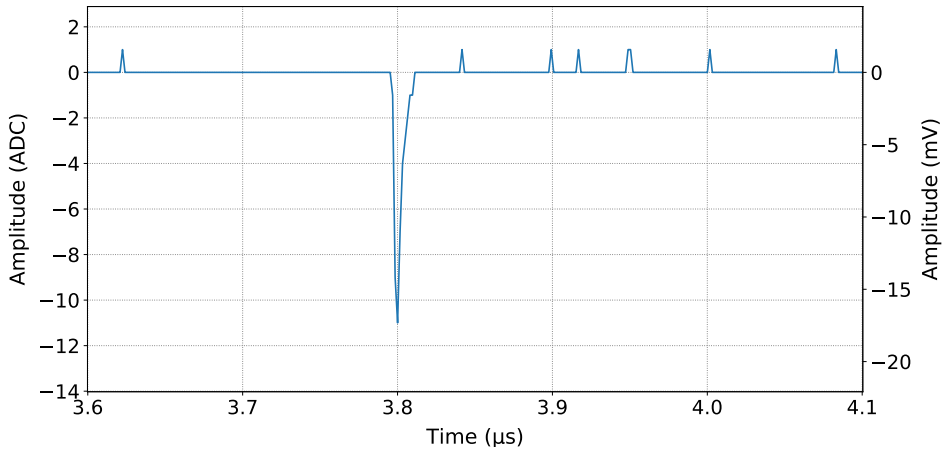

Figure 6.2: A section of the waveform of a Hamamatsu PMT at 1.0 MHz, with LED set at 2.2 V and PMT main voltage at 750 V, is shown. The mean lies at $-0.0014\,\mathrm{ADC} = -0.0022\,\mathrm{mV}$.

In Figure 6.2, a section of an obtained waveform for a main voltage of 750 V is shown. The plot presents the time in µs on the x-axis, which ranges from 3.5 to 4.0 µs, to illustrate the waveform baseline including a photon pulse. The left y-axis shows the received amplitude of the signal in ADC counts and the right y-axis shows the amplitude converted to mV. The baseline is very stable with no offset, making it easy to locate photon pulses. The mean of all the ADC values in the waveform results in $-0.0014\,\mathrm{ADC} = -0.0022\,\mathrm{mV}$. Another waveform taken for the main voltage setting 900 V is shown in Figure 6.3. The visible photon has a much higher pulse height than for 750 V and the mean results in $-0.1617\,\mathrm{ADC} = -0.2547\,\mathrm{mV}$. As the incident rate wasn't changed for both measurements, it is obvious that the pulse height increases when the main voltage is increased as well.
The pulse height histogram, shown in Figure 6.4, reflects the behavior just mentioned. The single photon peak moves towards higher negative pulse heights for increasing main voltage. The applied main voltages are written next to the color bar. The pedestal peak stays clearly at 0 ADC counts, which indicates a stable baseline with no offset. Its count rate does not decrease because the incident rate does not change and the same amount of photon pulses appears in the waveform. The incident rate is determined by applying and integrating a Gaussian distribution to the photon peak. As the settings and the setup weren't changed, the rate for all measurements lies around 1.0 MHz. In Figure 6.5, the center of the applied Gaussian distribution to the pulse height histograms is plotted against the main voltages. It shows clearly that the pulse height decreases for increasing voltage.

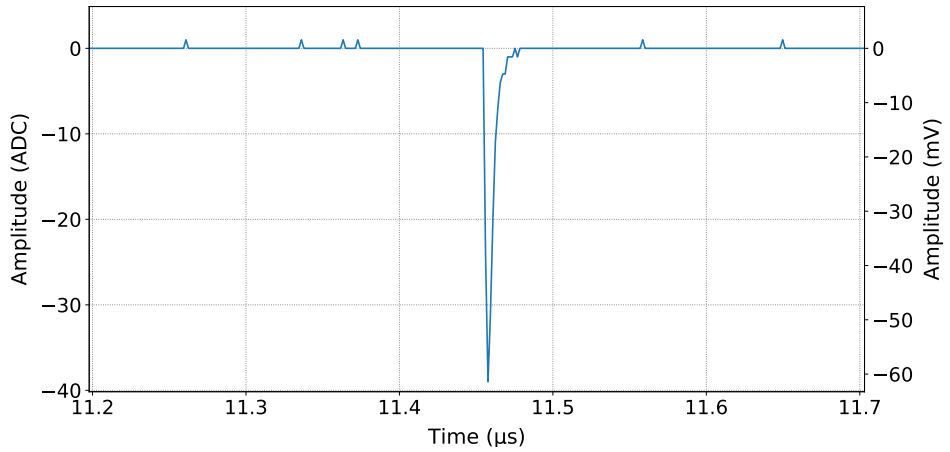

Figure 6.3: A section of the waveform of a Hamamatsu PMT at 1.0 MHz, with LED set at 2.2 V and PMT main voltage at 900 V, is shown. The mean lies at -0.1617 ADC $=$ -0.2547 mV.

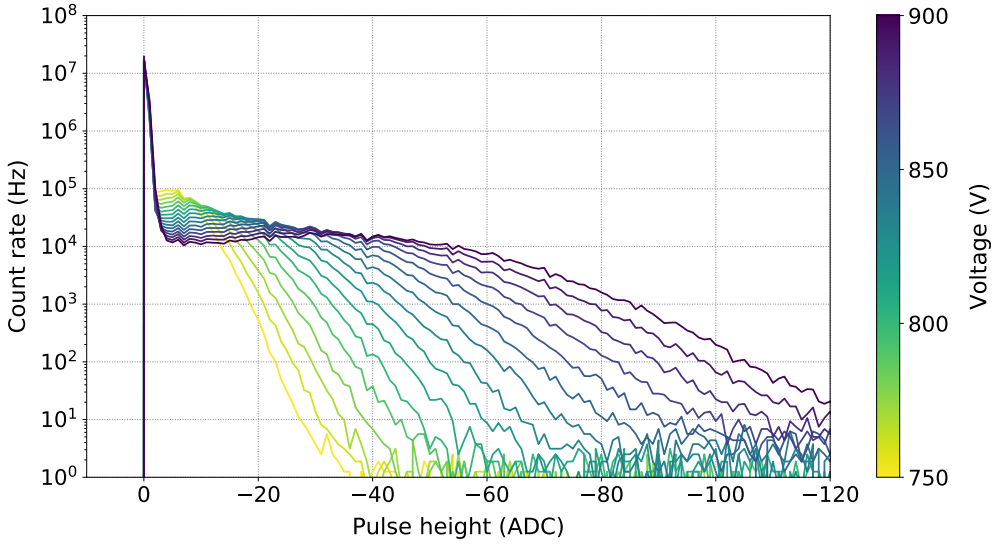

Figure 6.4: The pulse height histograms for a Hamamatsu PMT for different main voltage values with LED setting of 2.2 V is shown. The photon peak moves towards higher negative values with increasing main voltage.

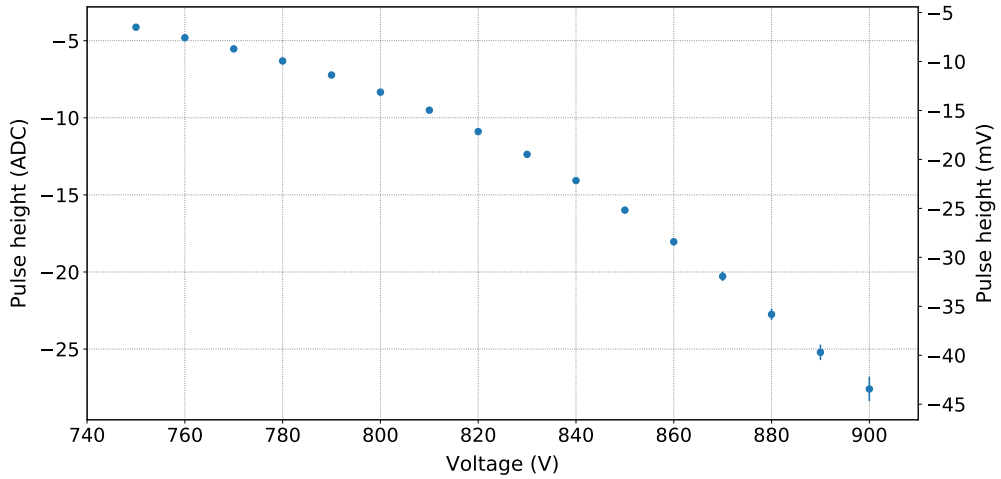

Figure 6.5: The center of the applied Gaussian distribution to the pulse height histograms is shown against the applied main voltages.

6.1.2 Investigation of the Pulse Shape

As mentioned before, it is important for various reasons to know what the photon pulse shape of the PMT looks like. To investigate the pulse shape of the Hamamatsu PMT, the waveforms of the voltage calibration measurements in subsection 6.1.1 were used.
A peak finding python program is applied to the waveform for one voltage. It looks at each data point and its neighboring points and compares their values. If the neighboring bins have a higher value than the investigated bin, it is defined as a minimum and thus a peak. The found peaks are sorted out and only peaks with a high pulse height are chosen. This is where the determined pulse height for each voltage from the pulse height histogram Figure 6.4 comes in. For each voltage this criterion is adjusted to match the data. The remaining high enough pulses are sorted out again. Since it is important that the pulse shape is not distorted by another pulse close by, only pulses with a certain distance to the next pulse are chosen. Then the remaining pulses are each normalized via their own peak maximum within 10 ns left and 350 ns right of the peak maximum. Last, the average pulse shape of the normalized pulses, that withstood the criteria, is determined.
These criteria reduce the amount of remaining pulses, which is why this process is done multiple times. As explained in section 3.3, the binary file is 2 GS long, which is arranged into smaller packets. To achieve a waveform, only one packet of 100 000 data points is taken. As the bin sampling was changed to 1.6 ns from 0.8 ns, the waveform is 160 µs instead of 80 µs long. To ensure high statistics, the process of establishing the pulse shape was done for 100 different packets of the

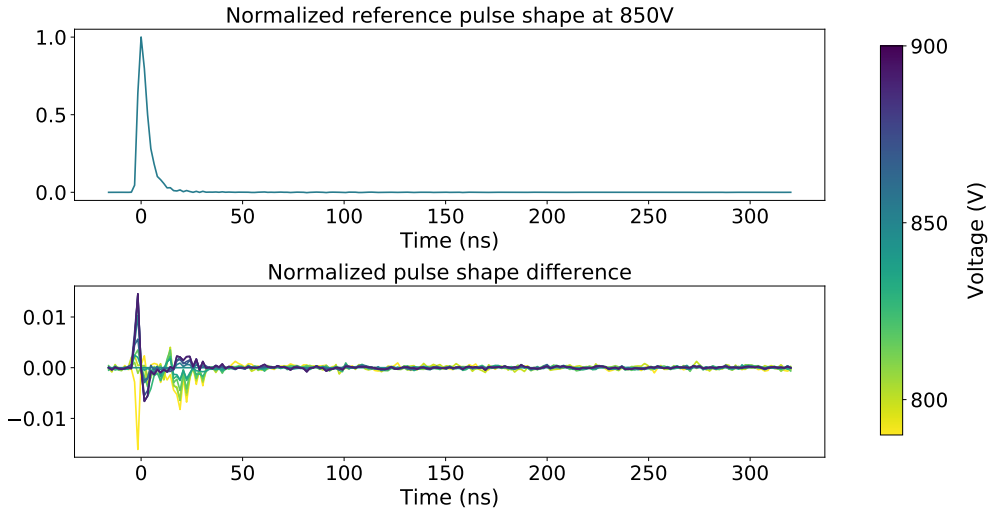

Figure 6.6: Upper: Normalized average pulse shape for a main voltage of 850 V used as a reference pulse shape. Lower: Difference of all the other pulse shapes to the reference one.

binary file for each voltage setting. This results in a high amount of pulses despite the criteria decreasing the amount found in one packet.
The result is shown in Figure 6.6. Since the average pulse shape of each voltage is very similar, the difference to a reference pulse shape at 850 V was plotted. The upper plot shows the normalized average pulse shape achieved for a main voltage of 850 V. The lower plot shows the very small difference of all the other voltages to the reference one. The color bar on the right allocates the different voltages from 790 V to 900 V. The voltages lower than 790 V had a too small pulse height (see Figure 6.5) for this investigation.

6.2 Calibration and Correlation Measurement

This section combines the knowledge that was achieved in this thesis for correlation measurements at the H.E.S.S. telescopes. Since the pulse height is not only dependent on the voltage applied to the PMT, as established in subsection 6.1.1, but also on other parameters, such as the cable lengths and temperature of the surroundings, the approach for the H.E.S.S. campaign was adjusted to this realization.
The setup used is shown in Figure 6.7. It consists of an LED with center wavelength of $\lambda = 465\,\text{nm}$ and a 75 µm pinhole, which is placed 3.3 m from the entrance window with the interference filter of 2 nm. The incoming filtered light is led through a

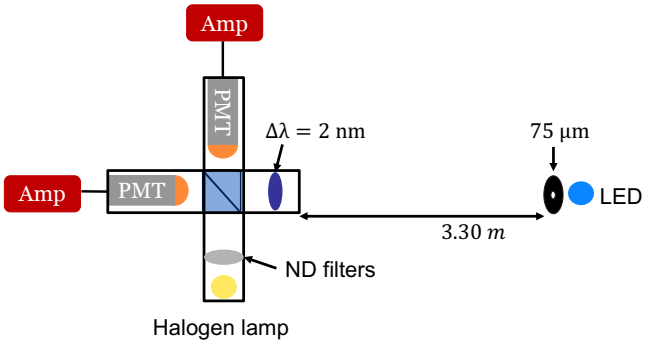

Figure 6.7: Schematic layout of the correlation setup. An LED with center wavelength of $\lambda = 465\,\text{nm}$ and a 75 µm pinhole is placed 3.3 m from the entrance window with the interference filter of 2 nm. The incoming filtered light is led through a 1-inch pinhole to a beamsplitter and the two Hamamatsu PMTs. A halogen lamp was installed with ND filters number 20, 6 and 2. The PMT signal is led to an amplifier and to the computer.

1-inch pinhole to a beamsplitter and the two Hamamatsu PMTs, PMT1 and PMT2. For reference measurements a halogen lamp was installed with ND filters number 20, 6 and 2.

Before starting the correlation measurement, the voltage applied to each PMT is set, in order to have similar gains and not to exceed the 100 µA current limit. For PMT1 the voltage was set to 840 V and for PMT2 to 880 V. Then a measurement without incoming light is taken, in order to determine a possible offset in the waveforms of the PMTs, which would have to be subtracted in the analysis. In this case an offset of zero was established.
The next step is to take a calibration measurement for the applied PMT voltages with the halogen lamp at low rate to make out single photon pulses. The voltage applied to the halogen lamp was set to 1.5 V. A section of the obtained waveforms for both PMTs is shown in Figure 6.8. To illustrate the waveform baseline including a photon pulse of each PMT, the x-axis ranges from 23.8 to 24.3 µs. The left y-axis shows the amplitude of the signal in ADC counts and the right y-axis converted to mV. The mean of the ADC values in the waveforms results in 0.03 ADC = 0.05 mV for PMT1 and 0.28 ADC = 0.44 mV for PMT2.
The pulse height histogram for both PMTs is shown in Figure 6.9. The pedestal peak stays clearly at zero ADC counts, which indicates a stable baseline with no offset. By applying and integrating a Gaussian distribution to the photon peak, the incident rate is determined to 0.15 MHz for both PMTs. The center and sigma of the Gaussian distribution for PMT1 are $\mu = -19.48$ and $\sigma = 14.47$. For PMT2 they result in $\mu = -20.16$ and $\sigma = 11.88$. These values are important for a simulation, which calculates the scaling factor of the $g^{(2)}$ function. They also depend on several

parameters, such as the cable lengths and temperature, which is why a calibration measurement has to be taken on site with the exact setup.
The average pulse shape for each PMT is then derived from the waveforms the same way as described in subsection 6.1.2. The result is shown in Figure 6.10 and is very similar for both PMTs.
After the calibration measurement, a correlation measurement is taken with the LED as light source. The voltage of the LED was set to 4.0 V, which results in a photon rate of about 200 MHz. To resemble the same photon rate for the reference measurement, the voltage of the halogen lamp was set to 4.2 V. In both cases the measuring time lasted one hour. The data was analyzed and the $g^{(2)}$ function plotted against time, which is shown in Figure 6.11. Although the baseline shows some fluctuations around one, the signal can be detected at about 110 ns. The reference measurement was subtracted from the signal to achieve the difference in order to subtract the correlated noise oscillations. Both $g^{(2)}$ functions are already multiplied by the correction factor. This factor is necessary because the scaling is different to the theory of Equation 2.8. Therefore, a waveform correlation simulation by Andreas Zmija is carried out with obtained waveforms and calculated μ and σ of the Gaussian distribution applied to the pulse height histogram. The correlation factor is calculated to be 2.439.
The next step is to determine the root mean square (RMS) of the received difference of both $g^{(2)}$ functions. It indicates the strength of fluctuations and is a quantitative investigation if all classifications are removed. The incident photon rate for both PMTs lies at $\dot{N}_0 = \dot{N}_1 = 200\,\mathrm{MHz}$. The time sampling was set to $\Delta t_{\mathrm{bin}} = 1.6\,\mathrm{ns}$ and the measuring time is $T_{\mathrm{t}} = 1\,\mathrm{h}$. With these values, the expected RMS can be calculated with the following equation:

$$\sigma_{g^{(2)}} = \frac{1}{\sqrt{\dot{N}_0 \cdot \dot{N}_1 \cdot \Delta t_{\mathrm{bin}} \cdot T_{\mathrm{t}}}} \cdot \sqrt{2} = 2.946 \cdot 10^{-6} \tag{6.1}$$

The RMS of the real $g^{(2)}$ function is calculated for the time range of 150 to 300 ns, since the peak signal lies around 110 ns. It results in $3.2 \cdot 10^{-6}$, which is slightly higher than the expected one, meaning that there is still some electrical noise in addition to the statistic photon fluctuations.
Another important value is the coherence time. For the measurement, it resembles the area of a Gaussian distribution fitted to the signal or difference peak. The coherence time of the difference for the measurement results in (0.137 ± 0.017) ps. In theory, it is calculated with Equation 2.4 and results in 0.36 ps, as in Equation 2.20. But the spatial loss factor of the setup has to be considered, which is calculated to 0.464. Multiplying the coherence time with the factor results in a new theoretical coherence time of 0.167 ps. Considering the error of the measurement result, it lies close to the theory, making it a successful measurement.

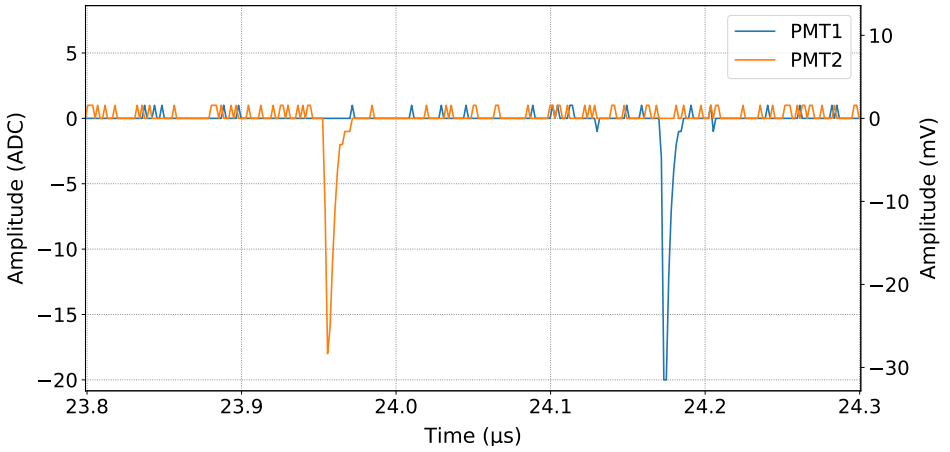

Figure 6.8: A section of the obtained waveforms for both Hamamatsu PMTs at 0.15 MHz, with halogen lamp set at 1.5 V is shown. The PMT main voltages are 840 V for PMT1 and 880 V for PMT2 and the mean lies at 0.03 ADC = 0.05 mV for PMT1 and 0.28 ADC = 0.44 mV for PMT2.

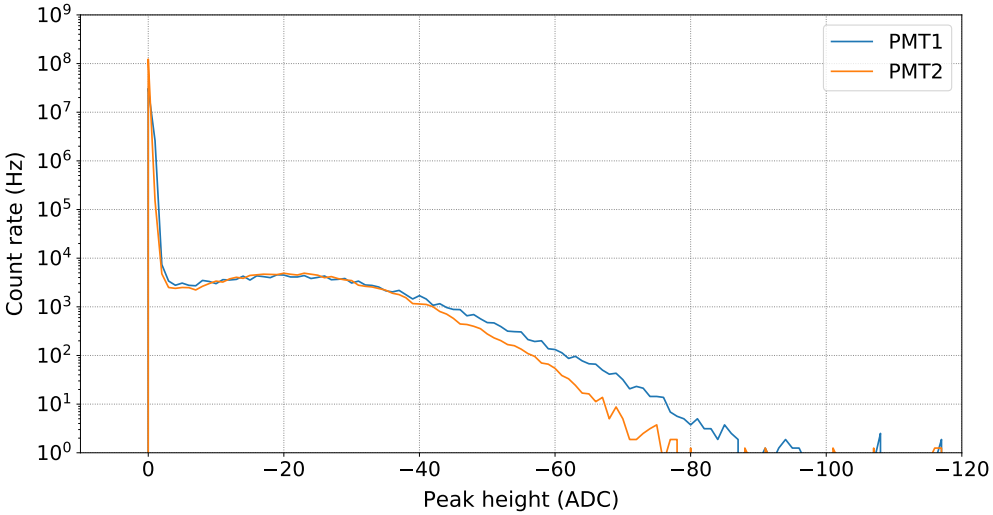

Figure 6.9: The pulse height histograms for both Hamamatsu PMT at 0.15 MHz with halogen lamp setting of 1.5 V is shown. The PMT main voltages are 840 V for PMT1 and 880 V for PMT2.

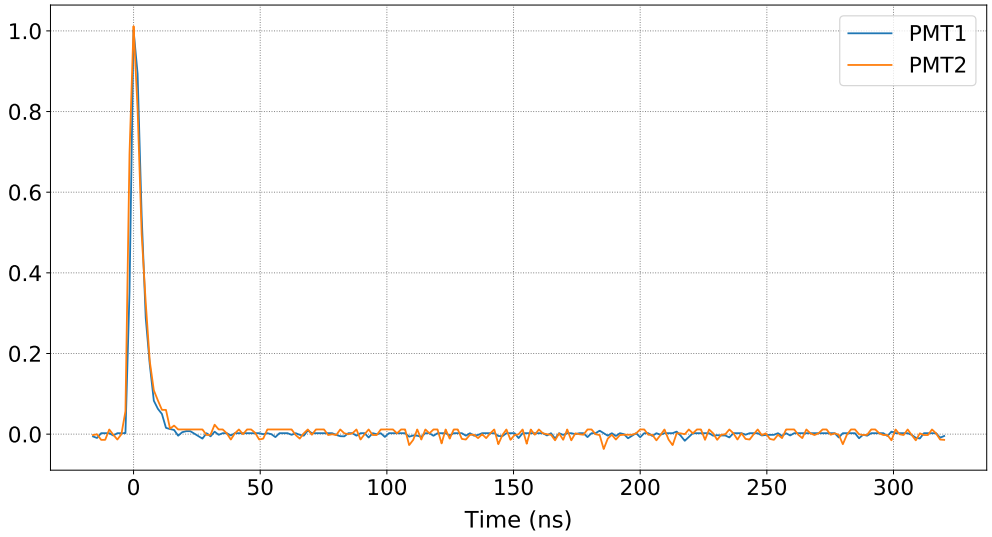

Figure 6.10: Normalized average pulse shape for both Hamamatsu PMTs for main voltages of 840 V for PMT1 and 880 V for PMT2.

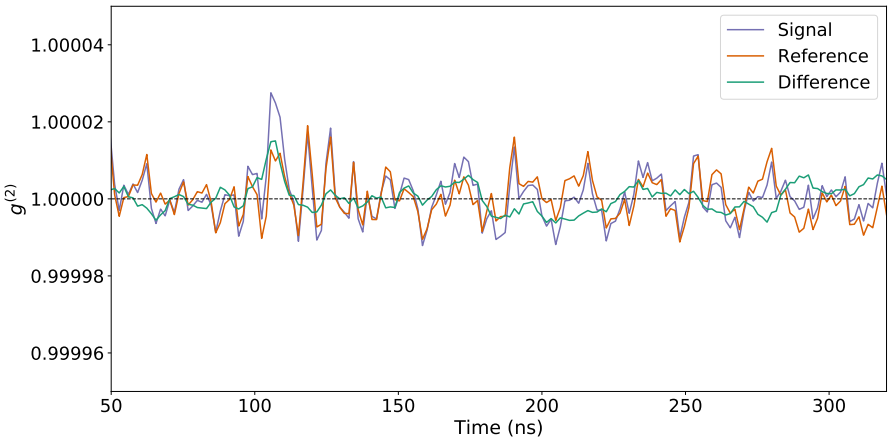

Figure 6.11: The obtained $g^{(2)}$ functions of the correlation measurement with the LED (blue) and the reference measurement with the halogen lamp (orange) are shown. The difference between the two functions is plotted in green.

Chapter 7

Conclusion

Within the scope of this thesis, improvements for rate measurements with the FlashCam and Hamamatsu PMTs were addressed, as well as developing a measurement procedure for the planned H.E.S.S. campaign.
The reasons for conducting systematic waveform investigations for the FlashCam PMT were the issues exposed in the results of the measurements conducted at the MST prototype in Berlin. The PMT showed saturation effects and its obtained waveform a baseline shift towards positive values for higher rates, which was assumed to stem from applying a base with only one voltage channel connection to the PMT. For investigations in the lab, rate measurements were conducted with an LED, ND filters to achieve various rates and the FlashCam PMT with a new base with two voltage channels. It was established that the calculated mean of the waveforms did not change significantly for higher rates as expected due to the increasing amount of photons pulses. This behavior is also reflected in the obtained pulse height histograms, where the photon peak doesn't shift to larger negative values.
Waveforms at different rates were simulated to compare the behavior of the baseline. The mean of the simulated waveforms indeed decreased with high rates. To solve this issue, a different amplifier, which is DC coupled, was installed in the setup. New measurements confirmed the expected performance of the obtained waveforms and pulse height histograms.
In addition, the incident rate was calculated by applying and integrating a Gaussian distribution to the photon peak of the pulse height histogram. This method is very accurate for low rates, where the photon peak still resembles a Gaussian shape. For high rates, it is not suitable due to multi photon events.
Due to low internal amplification of the FlashCam PMT, an amplifier with high amplification was used, which intensified unwanted electrical noise. Therefore, further measurements were carried out with the Hamamatsu PMT, which has a higher internal amplification. An amplifier with less amplification was installed,

which reduced electrical noise and created a more stable baseline in the waveforms. New waveforms investigations were conducted for various rates. The calculated mean of the waveforms decreased with higher rates, as proven in the simulations. Another method for determining the incident rate was developed using the calculated mean of the waveforms. It was determined that the mean of the waveform shows a linear relation to the intensity of the incident light regulated by the ND filters. The transmission was then converted to rate by only using the results of the Gaussian fit for low rates and applying a linear fit. Due to the linear behavior of the mean, it was possible to determine the incident rate for higher rates. In conclusion, a calibration measurement would have to be carried out before the actual correlation measurement.
For the calibration it is also important to know the performance of the PMT for various applied voltages. The voltage calibration consists of measurements with the Hamamatsu PMT for several different applied voltages but for consistent incoming photon rate. It was established that the pulse height increases for increasing main voltage. In addition, the average pulse shape of the PMT was investigated for the different main voltages, which only shows small differences.
The last step is to combine the achieved knowledge for the planned correlation measurements at the H.E.S.S. telescopes. An example of the measurement procedure was carried out, starting by applying the appropriate voltages to both PMTs individually. A calibration measurement for these voltages is taken at a low incident photon rate to obtain waveforms with single photon pulses. The pulse height histograms are also plotted to determine the center and sigma of the applied Gaussian distribution for a simulation to calculate the scaling factor of the $g^{(2)}$ function and the incident photon rates. After the calibration measurement, the correlation measurement is carried out, as well as a reference correlation measurement. For both measurements the $g^{(2)}$ function is plotted and multiplied by the correction factor. To subtract correlated noise, the difference of both functions was plotted. For analysis, the RMS of the difference is calculated and compared to the expected RMS giving a quantitative investigation of the electrical noise. To establish the coherence time, the area of a Gaussian distribution fitted to the signal peak of the $g^{(2)}$ function is calculated. Comparing the coherence time to the one in theory with considering the spatial loss factor makes a good indication for a successful measurement.

The next steps for the intensity interferometry research group at ECAP include preparing the final setups, which will be mounted to the H.E.S.S. telescopes for first tests on big telescopes and different baselines. This not only involves the rod assembly and framework for the PMTs, which is already in construction, but also improved electronics concerning less electrical noise, which are tested in the lab first.

The overall goal is to integrate an intensity interferometry system in km baseline Imaging Air Cherenkov Telescope arrays, such as CTA south, which would provide countless different baselines and achieve high-significant correlation signals. Conclusively, one can say that the concept of intensity interferometry provides a valuable insight into stellar astrophysics by enabling direct measurements of fundamental stellar parameters, such as the angular size of stars of the order of less than one mas, and a sharper view of our Universe.

Appendix A

List of Abbreviations

CE	Collection efficiency
CTA	Cherenkov Telescope Array
DE	Detection efficiency
ECAP	Erlangen Centre for Astroparticle Physics
FFT	Fourier transform
FWHM	Full width half maximum
H.E.S.S.	High Energy Stereoscopic System
HV	High voltage
LED	light-emitting diode
mas	milliarcseconds
MST	Medium-sized telescope
ND	Neutral density
PMT	Photomultiplier tube
QE	Quantum efficiency
RMS	Root mean square

Appendix B

List of Figures

Appendix C

List of Tables

Appendix D

Bibliography

[1] Dainis Dravins et al. Optical intensity interferometry with the cherenkov telescope array. *Astroparticle Physics*, 43:331 – 347, 2013. doi: 10.1016/j.astropartphys.2012.04.017.

[2] R. Hanbury Brown et al. The stellar interferometer at Narrabri Observatory I. A. description of the instrument and the observational procedure. 137:375, 1967. doi: 10.1093/mnras/137.4.375.

[3] R. Hanbury Brown et al. The Angular Diameters of 32 Stars. 167:121–136, 1974. doi: 10.1093/mnras/167.1.121.

[4] Mark Fox. *Quantum Optics an Introduction*. Oxford University Press, 2006.

[5] Robert Hanbury Brown and Richard Q. Twiss. *2. A Test of a New Type of Stellar Interferometer on Sirius*, pages 8 – 12. Harvard University Press, 31 Dec. 1979. doi: https://doi.org/10.4159/harvard.9780674366688.c4.

[6] Dravins, Dainis et al. Long-baseline optical intensity interferometry - laboratory demonstration of diffraction-limited imaging. *A&A*, 580:A99, 2015. doi: 10.1051/0004-6361/201526334.

[7] Dainis Dravins. *Chapter 1 Intensity Interferometry*, pages 1–13. 23 May 2016.

[8] W. Guerin et al. Temporal intensity interferometry: photon bunching in three bright stars. *Monthly Notices of the Royal Astronomical Society*, 472(4): 4126–4132, 2017. doi: 10.1093/mnras/stx2143.

[9] Davis John. Forty years of progress in long-baseline optical interferometry: 2005 robert ellery lecture. *Publications of the Astronomical Society of Australia*, 23:94–104, 2006. doi: 10.1071/AS06012.

[10] H.E.S.S. - The high Energy Stereoscopic System . `https://www.mpi-hd.mpg.de/hfm/HESS/pages/about/`. Accessed: 7.9.2020.

[11] ECAP. H.E.S.S. - The high Energy Stereoscopic System. https://ecap.nat.fau.de/index.php/research/gamma-ray-astronomy/h-e-s-s/. Accessed: 7.9.2020.

[12] quantum interactive. Coherence. https://interactive.quantumnano.at/advanced/molecular-beams/coherence/. Accessed: 10.9.2020.

[13] Andreas Zmija. Design and characterization of an intensity interferometer with thermal light sources. Masterarbeit, Friedrich-Alexander-Universität Erlangen-Nürnberg, 2018.

[14] F-Praktikum experiment 45: Photonenstatistik 2017. http://www.fp.fkp.uni-erlangen.de/fortgeschrittenenpraktikum/versuchsangebot-fuer-bsclanf/BSc-Versuchsanleitungen/B45.pdf. Accessed: 11.9.2020.

[15] Leonard Mandel and Emil Wolf. *Optical coherence and quantum optics*. Cambridge University Press, 1995.

[16] Katja Gumbert. Laborversuch zur Intensitätsinterferometrie mit dem Cherenkov-Teleskop IceAct . Bachelorarbeit, Friedrich-Alexander-Universität Erlangen-Nürnberg, 2019.

[17] Hamamatsu Photonics K.K. Photomultiplier Tubes - Basics and Application. https://www.hamamatsu.com/resources/pdf/etd/PMT_handbook_v3aE.pdf, 2007. Accessed: 12.10.2020.

[18] Hamamatsu Photonics K.K. Photomultiplier Tubes - Construction and Operating Charac- teristics Connections to External Circuits. https://wwwmu.mpp.mpg.de/docs/pmtconstruct.pdf., 1998. Accessed: 12.10.2020.

[19] Hamamatsu Photonics K.K. Photomultiplier Tube R12992-100, 2017. Accessed: 12.10.2020.

[20] Hamamatsu Photonics K.K. Photomultiplier Tubes and Photomultiplier Tube Assemblies R11265U Series / H11934 Series, 2019. Accessed: 12.10.2020.

[21] ORTEC. Model VT120 Fast Timing Preamplifier Operating and Service Manual, 2002. Accessed: 12.10.2020.

[22] FAST. TA1000B-x Fast, Very Low Noise Pulse / Timing Preamplifier User Manual, 2016. Accessed: 12.10.2020.

[23] FAST. TA1000B-10/-50/-100/-200. Accessed: 12.10.2020.

[24] SPECTRUM instrumentation. M4i.22xx-x8 - 8 bit Digitizer up to 5 GS/s, 2020. Accessed: 13.10.2020.

[25] S.O. Flyckt and C. Marmonier. Photomultiplier Tubes - Principles and Applications. http://www2.pv.infn.it/~debari/doc/Flyckt_Marmonier.pdf., 2002. Accessed: 15.10.2020.

[26] Frequenzplan. https://www.bundesnetzagentur.de/DE/Sachgebiete/Telekommunikation/Unternehmen_Institutionen/Frequenzen/Grundlagen/Frequenzplan/frequenzplan-node.html, October 2019. Accessed: 19.9.2020.

[27] COSMOS. Angular Diameter. https://astronomy.swin.edu.au/cosmos/A/Angular+Diameter. Accessed: 19.9.2020.

[28] How CTA Works. https://www.cta-observatory.org/about/how-cta-works/. Accessed: 19.9.2020.

[29] F. Zernike. The concept of degree of coherence and its application to optical problems. *Physica*, 5(8):785 – 795, 1938. doi: 10.1016/S0031-8914(38)80203-2.

[30] P.H van Cittert. Die Wahrscheinliche Schwingungsverteilung in Einer von Einer Lichtquelle Direkt Oder Mittels Einer Linse Beleuchteten Ebene. *Physica*, 1(1):201 – 210, 1934. doi: 10.1016/S0031-8914(34)90026-4.

[31] Norbert Wiener. Generalized harmonic analysis. *Acta Math.*, 55:117–258, 1930. doi: 10.1007/BF02546511.

[32] Joseph Zbilut and Norbert Marvan. The wiener-khinchin theorem and recurrence quantification. *Physics Letters A*, 372:6622–6626, 2008. doi: 10.1016/j.physleta.2008.09.027.

[33] ORTEC. Model 660 5-kV Detector Bias Supply Operating and Service Manual, 2002. Accessed: 08.10.2020.

[34] CAEN. DT55xxE 4 Channel HV Power Supply Family with Ethernet and USB User Manual, 2019. Accessed: 15.10.2020.

Acknowledgements

Throughout the process of this thesis I received a great deal of support from wonderful and competent people who I would like to thank:

Prof. Dr. Gisela Anton for giving me the opportunity to write my thesis at her department and her expertise in various meeting discussions.

Prof. Dr. Stefan Funk for welcoming me into the II (now AQO) research group.

Andreas Zmija for introducing me to the Physics of II and his assistance concerning measurements, brain storming and rubber duck debugging. It was an eventful year working at his side.

Adrian Zink for his technical support throughout all measurements.

Michael Wagenpfeil and **Tobias Ziegler** for their help with the manuscript of this thesis and sharing their knowledge along the way.

Sebastian Schmidt, not only for his programming skills, but also for his gardening advice and fun personality and **Franziska Eberle** for accompanying me on this journey until the last minute (writing her thesis simultaneously has its advantages) and for being a great friend.

My whole **working group** for a fun and productive atmosphere in the office, including all the jokes to lighten up the mood when necessary and the office quiz calendar to expand our general knowledge.

My parents for always being there for me, supporting me and showing genuine interest in the research I do, although they probably only see the vast universe when I tell them about it.

Statutory Declaration

I declare that I have developed and written the enclosed Master's Thesis completely by myself, and have not used sources or means without declaration in the text. Any thoughts from others or literal quotations are clearly marked. The Master's Thesis was not used in the same or in a similar version to achieve an academic grading or is being published elsewhere.

Erlangen, November 9, 2020

Naomi Vogel